Check for updates

PLANETARY SCIENCE

Postimpact evolution of the South Pole–Aitken basin revealed by Chang'e-4 and Chang'e-6

Yuqi Qian[1]*†, Wenlei Song[2]†, James Head[3], Mingyu Tian[1], Zhuang Guo[2], Harald Hiesinger[4], Carolyn H. van der Bogert[4,5], Le Zhang[6], Jingyou Chen[6], Wanfeng Zhang[6], Ziqing Li[7], Lingzhi Sun[8], Xiangsong Wang[1], Wei-Ran Li[1], Jiacheng Liu[1], Nicolas Dauphas[1], Yi-Gang Xu[6], Guochun Zhao[1,2]*

Copyright © 2026 The Authors, some rights reserved; exclusive licensee American Association for the Advancement of Science. No claim to original U.S. Government Works. Distributed under a Creative Commons Attribution License 4.0 (CC BY).

South Pole–Aitken (SPA) basin has recorded complex geological histories of the Moon. It is a critical region for solving lunar fundamental questions but remained unexplored until the Chang'e-4 and Chang'e-6 missions of China. Their in situ measurements and the Chang'e-6 samples provided the first ground truth for the SPA evolution. On the basis of these constraints, we found that the SPA impact occurred ~4.34 billion years ago, generating a thick melt sheet that differentiated to form moderately magnesium (Mg)–rich norites. They are exposed at the SPA central peaks and currently investigated by the Chang'e-4 mission in Von Kármán crater, transported by the Finsen impact to the site. Highly Mg-rich materials were found within SPA, likely products of Mg-suite magmatism, including those exposed at the Apollo western peak ring. They were initially excavated by the Apollo impact at ~4.2 billion years ago and delivered to the Chang'e-6 site by the Chaffee S impact. A series of other events occurred in the SPA basin subsequently (e.g., the Orientale impact ~3.87 billion years ago); all of them shaped the architecture of the Moon's largest impact basin.

INTRODUCTION

Impact cratering is the dominant exogenic geological process on terrestrial planets. The Moon preserves one of the best impact records in the Solar System, without extensive modification. Lunar bombardment, especially in its early history, substantially controlled its evolution and shaped the surface landforms. To date, 74 impact basins (*1*) and >1 million craters with diameters over 1 km have been identified on the Moon (*2*). Among these impact features, the South Pole–Aitken (SPA) basin is the largest (2050 km by 2400 km), deepest (~12 km), and oldest (Fig. 1, A to C). Its formation may have triggered global mantle convection that migrated KREEP elements to the nearside, dramatically altering the Moon's evolution and creating its nearside-farside dichotomy (*3*). For such a gigantic event, impact simulations indicate that its transient cavity could readily reach the deep crust and even the upper mantle (>80 km) (*4*). These deep components were likely to be dispersed across the basin (*5*). Together, these factors make SPA a critical region to constrain the origin of the lunar dichotomy, the composition of the lunar mantle, and the timing of the Late Heavy Bombardment (*6*).

Thus, the SPA basin has been proposed as a high-priority sampling region for decades (*6*). However, in situ exploration of SPA has not been implemented until the recent China National Space Administration (CNSA)'s Chang'e-4 (CE-4) and Chang'e-6 (CE-6) missions to the interior of SPA, and the National Aeronautics and Space Administration's (NASA) Commercial Lunar Payload Services (CLPS) missions Odysseus and Athena to the rim of SPA at the south pole. SPA will also be the landing site for the upcoming Chang'e-7 (CE-7), NASA's Artemis IV, and multiple CLPS missions to the South Pole, as well as the Endurance rover planning to traverse across SPA. Among them, the CE-4 mission was launched on 08 December 2018, and landed on the eastern Von Kármán crater (177.588°E, 45.457°S), northwestern SPA (Fig. 1A). The deployed Yutu-2 rover has traveled >1650 m as of January 2026 (Fig. 2, A and B). The CE-6 mission was launched on 03 May 2024 and landed on the southern Apollo basin, northeastern SPA (153.983°W, 41.642°S) (Fig. 1A). Approximately ~1935.3 g of lunar soil was collected by CE-6, representing the first farside materials from known locations. These two in situ missions have provided unprecedented opportunities and ground truth to assess the geological history of the basin. Landing on mare basalts, CE-4 (*7*) and CE-6 (*8*) basalts have offered clues to mare volcanism in SPA, and provided evidence that its underlying mantle was modulated by this impact (*9*). Even more information will be carried by the impact materials of SPA and other subsequent impacts. Although buried by later basalts at ~3.6 billion years ago (Ga) (*7*) and ~2.8 Ga (*10*, *11*), the continuous impact mixing would transport these impactites to the CE-4 and CE-6 sites, shedding light on the geological evolution of the Moon's most ancient basin.

Responding to the giant impact (*4*), SPA has one of the most complex geological histories on the Moon. From the basin center toward its exterior, it is characterized by compositional zones of (i) SPA Compositional Anomaly (SPACA), (ii) Mg-Pyroxene Annulus (MPA), and (iii) Heterogeneous Annulus (HA) (Fig. 1, A to C) (*5*). SPACA is abundant in intermediate-Ca, Fe pyroxenes, overlying the MPA materials, which have been interpreted to be products of melt sheet differentiation (*12*) or cryptomare volcanism (*5*). Mg-rich materials are widespread at crater central peaks in the SPACA and MPA. Their origin is debated, ranging from melt sheet differentiation to deep interior compositions (*5*). The CE-4 and CE-6 sites are highly likely to contain fragments from these distinct compositional

[1]NWU-HKU Joint Center of Earth and Planetary Sciences, Department of Earth and Planetary Sciences, The University of Hong Kong, Pokfulam, Hong Kong, China. [2]NWU-HKU Joint Center of Earth and Planetary Sciences, National Key Laboratory of Continental Evolution and Early Life, Department of Geology, Northwest University, Xi'an, China. [3]Department of Earth, Environmental and Planetary Sciences, Brown University, Providence, RI, USA. [4]Institut für Planetologie, Universit¨at Münster, Münster, Germany. [5]European Space Research and Technology Centre, Directorate of Human and Robotic Exploration, European Space Agency, Noordwijk, Netherlands. [6]GIGCAS-HKU Joint Laboratory of Chemical Geodynamics, Guangzhou Institute of Geochemistry, Chinese Academy of Sciences, Guangzhou, China. [7]School of Earth and Space Sciences, Peking University, Beijing, China. [8]Hawai'i Institute of Geophysics and Planetology, University of Hawai'i at Mānoa, Honolulu, HI, USA.
*Corresponding author. Email: yuqiqian@hku.hk (Y.Q.); gzhao@hku.hk (G.Z.)
†These authors contributed equally to this work.

Downloaded from https://www.science.org on November 18, 2026

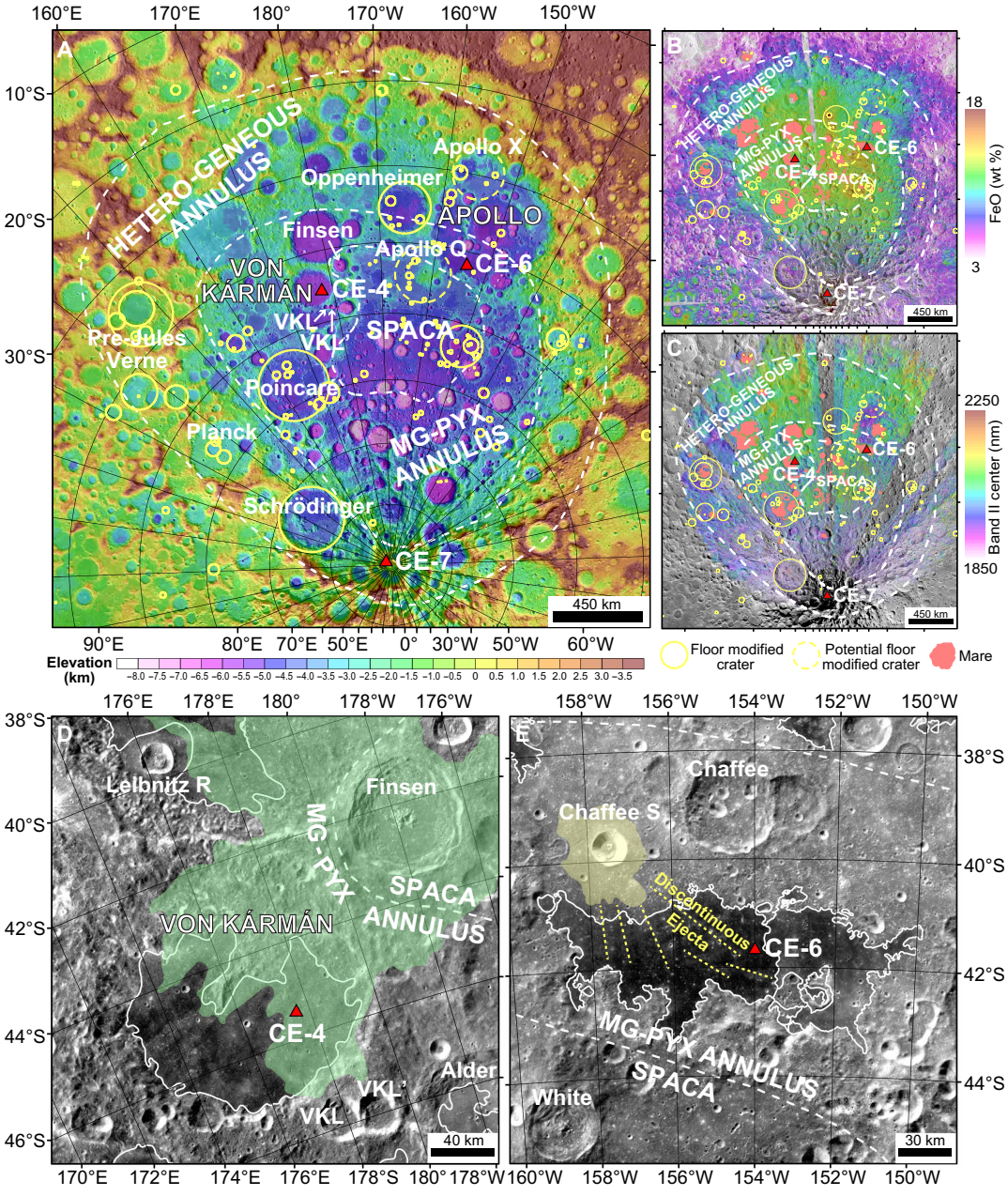

Fig. 1. CE-4, CE-6, and CE-7 landing sites in SPA. (**A**) Elevation of SPA. The white dashed lines indicate the compositional zones of SPA. The basemap is the LRO LOLA DEM. (**B**) FeO abundance of SPA based on Clementine UVVIS data. (**C**) Band II (BC2) centers of SPA based on Moon Mineralogy Mapper (M^3) data. (**D**) The CE-4 site in the eastern Von Kármán crater, to the southwest of the Finsen crater, on its continuous ejecta blanket (green area). VKL and VKL′ represent Von Kármán L and L′ craters, respectively. (**E**) The CE-6 site in the southern Apollo basin, to the southeast of Chaffee S crater, on its discontinuous ejecta (yellow dashed lines; the yellow area represents the continuous ejecta). The basemaps of (D) and (E) are the CE-2 CCD DOM.

zones. The identification and characterization of these enigmatic materials are extremely valuable if their provenance were fully constrained so that they could help to improve the understanding of the formation and evolution of SPA.

Thus, we present a synthetic study of the CE-4 and CE-6 missions from two regions in SPA, combining in situ measurements, returned samples, and orbital observations. We aim to better understand the material characteristics at the CE-4 and CE-6 landing sites and construct the postimpact geological history of SPA based on their ground truth. These results point to a series of outstanding questions for future exploration of this giant impact basin.

RESULTS

CE-4 and CE-6 lunar soil provenance

The ejecta decay models of Sharpton (*13*) and Pike (*14*) were used to compute the ejecta thickness of impact craters and basins, respectively, both calibrated to lunar observation data. Here, primary ejecta

Downloaded from https://www.science.org on November 18, 2026

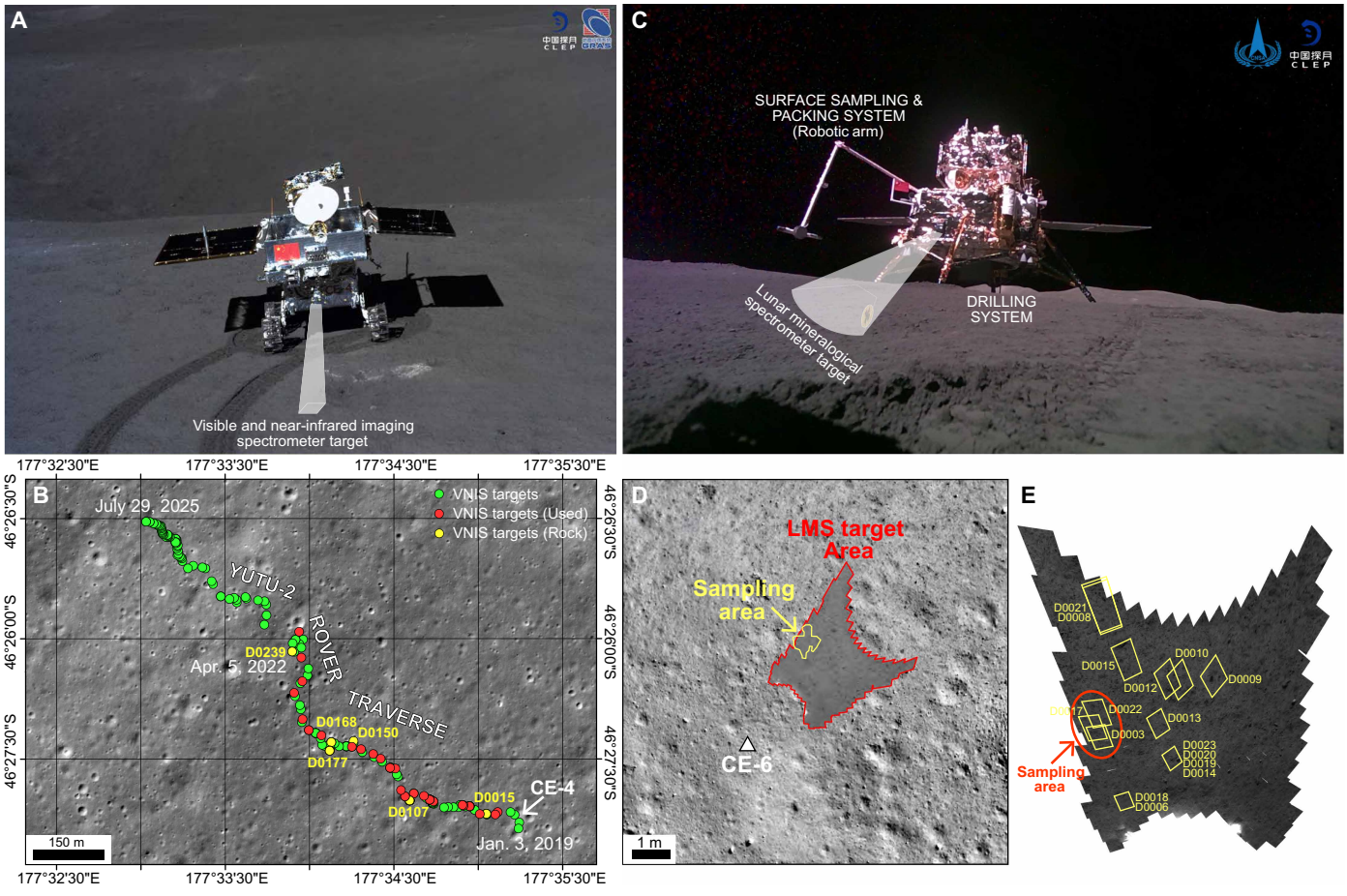

Fig. 2. CE-4 and CE-6 investigation and measurement regions. (**A**) The Yutu-2 rover at the CE-4 site. VNIS is installed on the front platform of Yutu-2. (**B**) CE-4 VNIS investigation targets. The red and yellow dots represent the soil and rock data used, respectively. The green dots represent all VNIS observations as of 29 July 2025. The basemap is LROC NAC image M1472592857. (**C**) Sampling mechanism of CE-6. Samples used here were collected from the surface by the robotic arm from a depth of ≤3 cm. (**D**) CE-6 sampling site. The white triangle represents the lander. The sampling and LMS investigation area are very homogeneous. The basemap is a CE-6 LCAM image. (**E**) CE-6 LMS investigation targets. CE6-D0003/D0017/D0022 covered the surface sampling locations. The basemap is from the multispectral full-view mode of LMS at 750 nm.

represents materials directly excavated and delivered to the investigating site by the impact event; total ejecta represents the sum of primary ejecta and the redistributed local materials by the ballistic excavation, deposition, and mixing of primary ejecta (*15*). Located on the eastern floor of the Von Kármán crater (diameter = 186 km), the CE-4 site is on the continuous ejecta of the Finsen (diameter = 73.1 km) crater. The surface materials investigated by CE-4 are predominantly from Finsen, whose ejecta covers the northeastern Von Kármán crater (Fig. 1D). Using Sharpton's (*13*) ejecta model indicates that ~4.6 m of Finsen primary ejecta were emplaced at the CE-4 landing site (Fig. 3A), on top of all basalts erupted at ~3.6 Ga (*7*). Besides, Von Kármán L and L′ (VKL and VKL′) craters could deliver >1.0 m of primary ejecta to the landing site. However, crater size–frequency distribution (CSFD) measurements suggest that these two craters have ages around 4.0 Ga, predating local mare eruptions, and thus their ejecta underlie CE-4 basalts and Finsen ejecta (~3.1 Ga) (*16*). Therefore, the materials studied by CE-4 are primarily from the Finsen crater (Figs. 1D and 3A).

At the CE-6 site, as the only location with returned farside samples, a comprehensive procedure was used to constrain the provenance of its soils, following Qian *et al.*'s (*17*) approach (see Materials and Methods). For >1 million craters investigated over the Moon, 67 craters postdating the CE-6 mare basalts (~2.83 Ga) (*10*, *11*) are able to deliver 0.1 cm of primary ejecta. They were further studied for their contribution to the landing site (tables S2 to S5). Figures 3 and 4 show the source craters that were able to deliver >2 vol % local mare materials (originated from the CE-6 mare unit) or >0.1-cm exotic nonmare materials (originated outside the CE-6 mare unit) to the CE-6 site (see also Table 1). Among them, five craters (Local_11268, 11380, 11379, 10939, and 11304) affected local basalts, contributing ~45.4 cm of primary ejecta, occupying 48.7/55.3 vol % (results of young and old estimation models, respectively, hereafter) of CE-6 soils. Together with other neighboring craters, 54.0/61.3 vol % of the ejecta materials originated from local basalts (<5 km) (Fig. 3D). Distant mare components are rare (<0.2 to 0.3 vol %). The other 38.4/45.7 vol % soils are nonmare materials (Figs. 3B and 4). Chaffee S, situated at the Apollo western peak ring, is the most significant nonmare source (Fig. 3C). Its discontinuous ejecta overlies the Apollo southern mare unit visually (Fig. 1E), indicating that Chaffee S postdates the CE-6 mare basalts. Approximately 15.0 cm (16.1/18.2 vol %) of Chaffee S primary ejecta was incorporated into the CE-6 soils. Local_3018 is perhaps the second-highest exotic source. However,

Downloaded from https://www.science.org on November 18, 2026

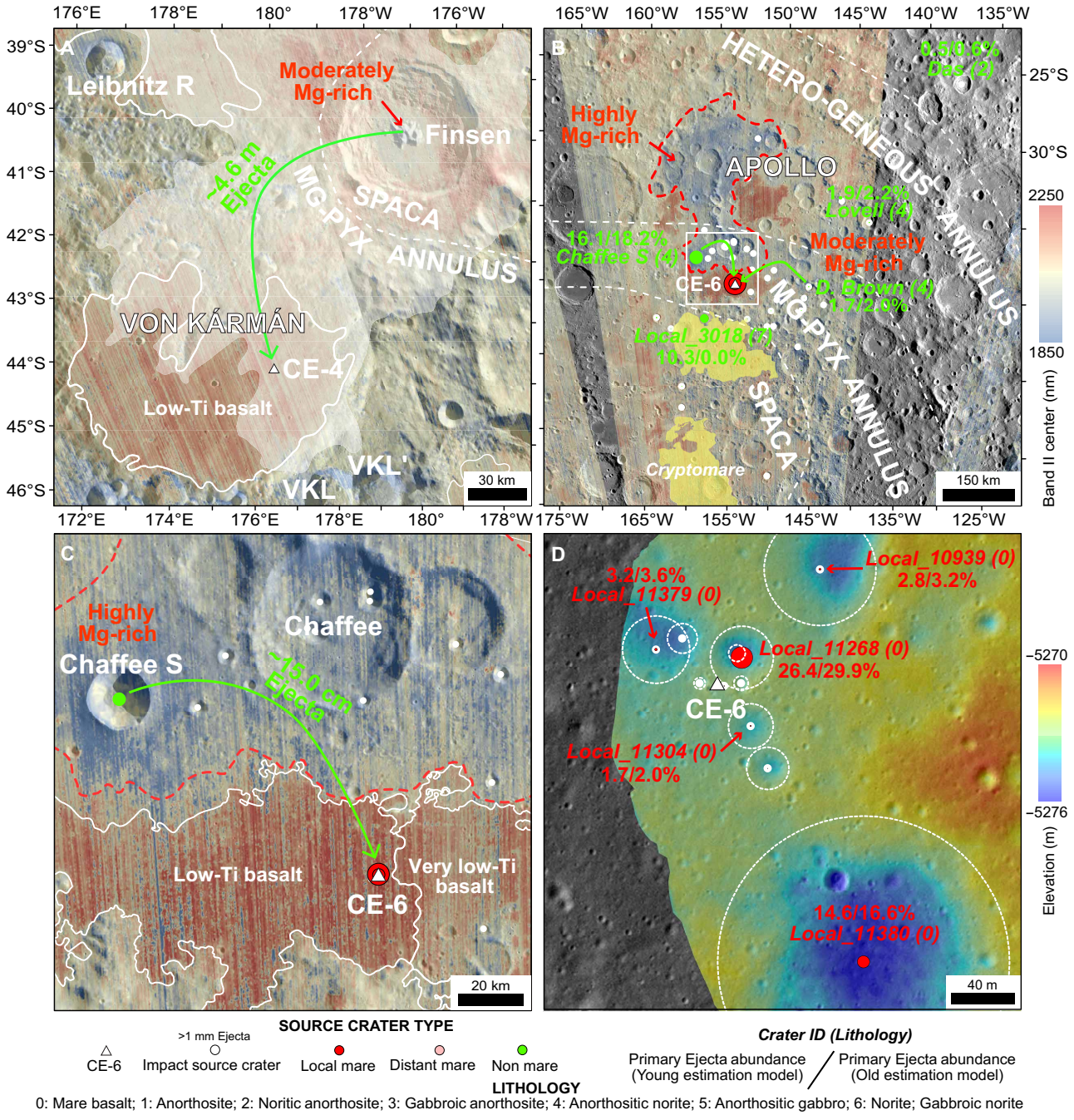

Fig. 3. Provenance of the CE-4 and CE-6 lunar soils. (**A**) CE-4 landed on the continuous ejecta deposit of Finsen (white area). Materials investigated by the Yutu-2 rover are predominantly from its moderately Mg-rich ejecta (~4.6 m of primary ejecta). VKL and VKL′ represent Von Kármán L and L′ craters, respectively. (**B** and **C**) Distal craters contributed >0.1 vol % nonmare materials to the CE-6 site. Approximately 16.1/18.2 vol % of the materials are from the highly Mg-rich Chaffee S crater. The basemap of (A to C) is M^3 BC2 centers. (**D**) Craters transported >2 vol % of local mare materials to the CE-6 site, primarily (>50 vol %) from local basalts <5 km from the landing site. The basemap of (D) is the CE-6 LCAM DEM overlaying the LROC NAC image. The diameter of circles represents the relative ejecta contribution from each source crater. Labels of Local_11380 (0), etc., indicate the crater ID and their lithology in our database (tables S2 to S5). The lithology is based on the mineral abundances obtained from Kaguya MI data (*30*, *31*).

Downloaded from https://www.science.org on November 18, 2026

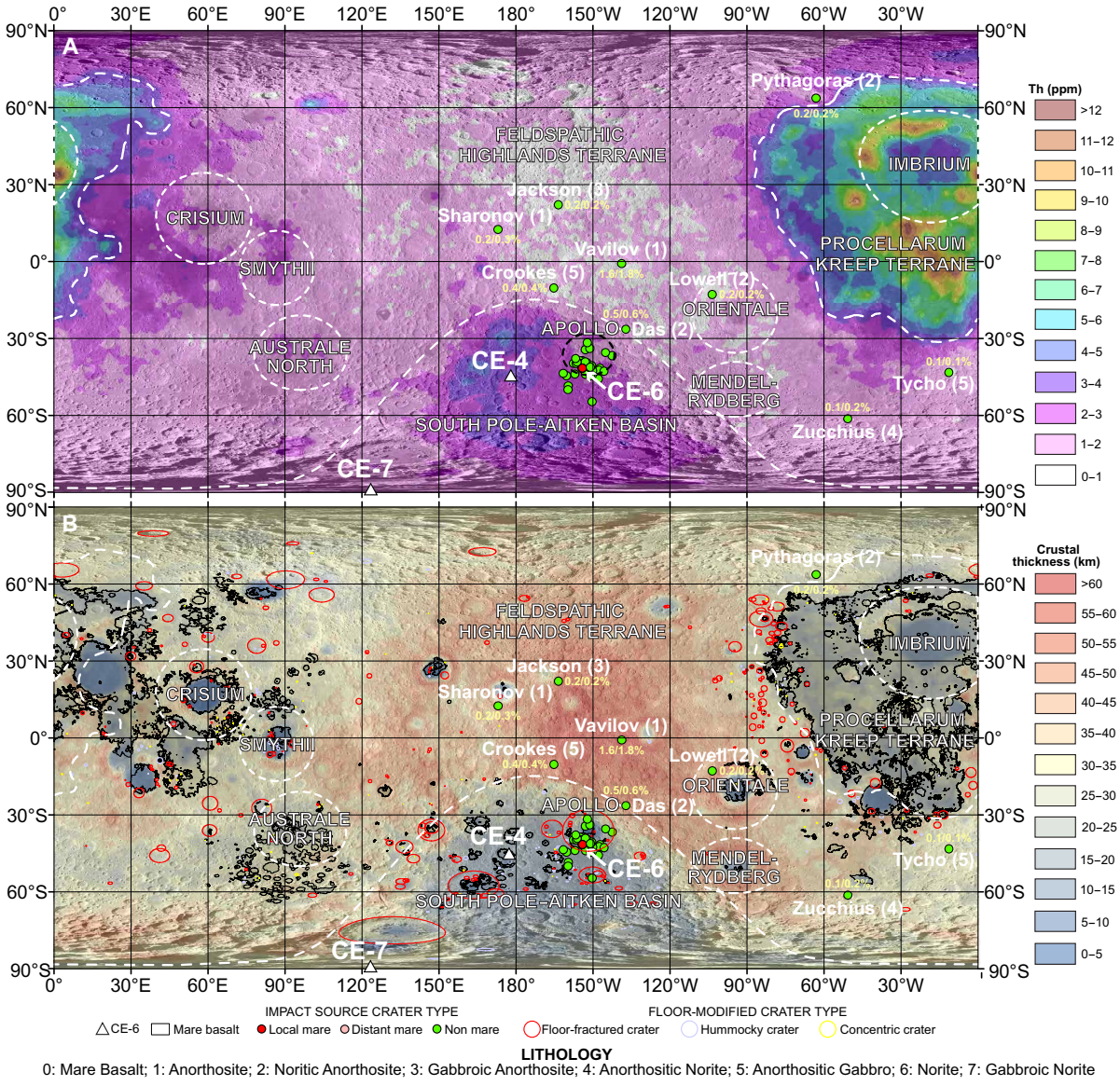

Fig. 4. Impact craters able to contribute >0.1 vol % of nonmare materials, and impact basins able to contribute >5 m of primary ejecta to the CE-6 landing site. (**A**) Lunar Prospector thorium abundance of the Moon and major crustal terranes (*55*). (**B**) Crustal thickness of the Moon (*45*) and the distribution of floor-modified craters (*46*). These special impacts are indicative of subsurface intrusions, mainly distributed in regions with intermediate-thick crust. The lithology is based on the mineral abundances obtained from Kaguya MI data (*30*, *31*).

its age (2.8/3.4 Ga) is close to that of local basalts, making its formation order ambiguous. If postdating local basalts, it will provide ~9.6 cm (10.3 vol %) of primary ejecta. In addition, seven critical sources are located in the Feldspathic Highlands Terrane (FHT), characterized by anorthosite lithology; these include the Vavilov, Crookes, Sharonov, Lowell, Jackson, and Tycho craters (Fig. 4). Pure anorthosite (PAN) lithologies were reported for all of these craters previously (table S4) (*18*). In total, ~2.5 cm (2.7/3.2 vol %) of anorthosite might be mixed into the CE-6 soils.

CSFD, crater degradation method (CDM, text S1), and crater morphology method (CMM, text S2) were used to determine the ages of all nonnegligible source craters (table S3). The age histogram was constructed (Fig. 5, A to C, and table S5). For both age estimation models, the age distribution of impact materials has multiple peaks, mainly from Chaffee S, in addition to Local_3018, Vavilov, D. Brown, and Lovell. All these craters are older than 1000 million years ago (Ma). Local craters <5 km from the CE-6 site dominate the young impact materials, including Local_11268 (18 Ma), 11380 (620 Ma), 11379 (130 Ma), 10939 (150 Ma), and 11304 (45 Ma) in the last 1000 Ma.

All the aforementioned craters postdating local basalts are able not only to transport local mare materials (listed in Table 1 and table S4) but also to excavate preexisting basin materials buried by maria. To estimate the potential contribution of such basin materials, the ejecta thickness of all basins (*1*) was computed on the basis of Pike's (*14*) model (table S6) after spherical correction due to the curvature

Downloaded from https://www.science.org on November 18, 2026

Table 1. Characteristics of impact source craters that are able to deliver >2 vol % local mare materials or >1 mm exotic nonmare materials to the CE-6 landing site.

Impact crater ID	Lon. (°)	Lat. (°)	Diameter (km)	Primary ejecta thickness (cm)	Primary ejecta abundance young/old (vol %)	Impact age	Impact target	SPA compositional zone
Local mare material								
Local_11268	−153.982	−41.641	0.040	24.6	26.4/29.9	18 + 7/−2 Ma (CDM)* 20–50 Ma (CMM)*	Apollo southern mare	Mg-Pyx. Ann. (SPAT)
Local_11380	−153.979	−41.647	0.183	13.6	14.6/16.6	620 + 240/−20 Ma (CDM)* 546–1092 Ma (CMM)*	Apollo southern mare	Mg-Pyx. Ann. (SPAT)
Local_11379	−153.985	−41.641	0.042	3.0	3.2/3.6	130 + 40/−0 Ma (CDM)* 128–255 Ma (CMM)*	Apollo southern mare	Mg-Pyx. Ann. (SPAT)
Local_10939	−153.980	−41.639	0.070	2.6	2.8/3.2	150 + 40/−10 Ma (CDM)* 110–220 Ma (CMM)*	Apollo southern mare	Mg-Pyx. Ann. (SPAT)
Local_11304	−153.982	−41.642	0.028	1.6	1.7/2.0	45 + 5/−10 Ma (CDM)* 45–90 Ma (CMM)*	Apollo southern mare	Mg-Pyx. Ann. (SPAT)
Exotic nonmare material								
Local_3051 (Chaffee S)	−157.5	−39.8	19.5	15.0	16.1/18.2	1840 + 290/−290 Ma (CSFD) 2790 + 230/−280 Ma (CSFD)	Apollo western peak ring	Mg-Pyx. Ann. (SPAT)
Local_3018	−156.9	−44.0	17.4	9.6	10.3/0.0	2750 + 380/−570 Ma (CSFD) 3350 + 140/−330 Ma (CSFD)*	Apollo southern rim	SPACA (SPAT)
Local_86 (Lovell)	−142.4	−36.8	28.7	1.8	1.9/2.2	1750 + 150/−150 Ma (CSFD)	Apollo eastern rim	Heterogeneous Ann. (SPAT)
Local_2007 (D. Brown)	−147.2	−41.7	15.8	1.6	1.7/2.0	2540 + 330/−360 Ma (CSFD)	Apollo southeastern rim	Mg-Pyx. Ann. (SPAT)
Distant_277341 (Vavilov)	−138.8	−0.9	96.4	1.5	1.6/1.8	1260 + 70/−70 Ma (CSFD) 1860 + 120/−120 Ma (CSFD)	Nectarian terra unit	FHT
Distant_277895 (Das)	−137.1	−26.5	35.8	0.5	0.5/0.6	658 + 64/−64 Ma (CSFD) 719 + 0/−0 Ma (RA)	SPA northeastern ring	FHT/SPAT
Distant_277431 (Crookes)	−165.1	−10.4	49.2	0.3	0.4/0.4	488 + 0/−0 Ma (RA)	Nectarian terra unit	FHT
Distant_805121 (Sharonov)	173.1	12.3	75.9	0.2	0.2/0.3	2,200 + 300/−300 Ma (CSFD)	Nectarian terra unit	FHT
Distant_277546 (Lowell)	−103.4	−13.0	63.1	0.2	0.2/0.2	374 + 28/−38 Ma (CSFD) 652 + 47/−47 Ma (CSFD)	Orientale Montes rook formation	FHT
Distant_134734 (Jackson)	−163.3	22.0	71.5	0.2	0.2/0.2	147 + 0/−0 Ma (RA)	Nectarian terra unit	FHT
Distant_1119 (Pythagoras)	−63.0	63.6	127.6	0.1	0.2/0.2	2130 + 160/−160 Ma (CSFD) 2680 + 280/−320 Ma (CSFD)	Pre-Nectarian terra unit	PKT
Distant_1147236 (Zucchius)	−50.6	−61.4	64.6	0.1	0.1/0.2	1670 + 230/−230 Ma (CSFD)	Orientale Hevelius formation	FHT/PKT

(*Continued*)

Downloaded from https://www.science.org on November 18, 2026

(*Continued*)

Impact crater ID	Lon. (°)	Lat. (°)	Diameter (km)	Primary ejecta thickness (cm)	Primary ejecta abundance young/old (vol %)	Impact age	Impact target	SPA compositional zone
Distant_434331 (Tycho)	−11.2	−43.3	83.2	0.1	0.1/0.1	58 + 3/−3 Ma (CSFD) 124 + 12/−12 Ma (CSFD)	Nectarian terra unit	FHT
Exotic basin material								
Orientale	−94.8	−20.1	937	29.3 m	Beneath local basalt	3.87 Ga (Sample)	Nectarian terra unit	FHT
Imbrium	−18.5	37.0	1321	22.5 m	Beneath local basalt	3.92 Ga (Sample)	Nectarian terra unit	PKT
Oppenheimer	−166.0	−35.4	206	5.9 m	Beneath local basalt	4.04 Ga (CSFD)	Nectarian terra unit	SPAT
Crisium	58.4	16.8	1076	6.8 m	Beneath local basalt	4.07 Ga (CSFD)	Nectarian terra unit	FHT
Mendel-Rydberg	−94.6	−49.8	650	12.9 m	Beneath local basalt	4.13 Ga (CSFD)	Nectarian terra unit	FHT/SPAT
Apollo	−151.7	−36.1	492	/	Beneath local basalt	~4.2 Ga (Sample)	SPA northeastern ring	SPAT
Smythii	86.9	−2.5	878	6.3 m	Beneath Apollo	4.26 Ga (CSFD)	Pre-Nectarian terra unit	FHT
Australe North	96.0	−35.5	880	7.7 m	Beneath Apollo	Pre-Nectarian period	Pre-Nectarian terra unit	FHT
SPA	−169.0	−53.0	2050 × 2400	/	Beneath Apollo	4.34 Ga (Sample)	Pre-Nectarian terra unit	/

Notes: CSFD, CDM, CMM, RA, and Sample indicate ages determined by CSFD measurements, crater degradation, crater morphology, rock abundance methods, and isotopic measurements of returned samples. Those marked by stars were determined in this study. See tables S3 and S6 for references and more details.

of the Moon. Orientale (~29.3 m), Imbrium (~22.5 m), Mendel-Rydberg (~12.9 m), Australe North (~7.7 m), Crisium (~6.8 m), Smythii (~6.3 m), and Oppenheimer (~5.9 m) could each contribute >5 m of primary ejecta (Fig. 4). The ages of these basins were constrained previously by CSFD or collected samples (Table 1): Smythii (4.26 Ga) (*19*), Mendel-Rydberg (4.13 Ga) (*19*), Oppenheimer (4.04 Ga) (*20*), Crisium (4.07 Ga) (*19*), Imbrium (3.92 Ga) (*21*), and Orientale (3.80 to 3.81 Ga) (*19*, *22*). Australe North is very ancient, with extremely degraded morphologies and has not been dated by CSFD. Landing within the Apollo basin, materials from the Apollo and SPA basins were also very likely collected by CE-6. For SPA, CSFD measurements suggested an age of 4.26 to 4.31 Ga (*19*, *20*). The isotopic dating of NWA2995 suggested an SPA impact at 4.33 Ga (*23*), concurrent with the global magmatic event at 4.35 Ga (*24*), older than the estimates of 4.25 Ga based on Apollo 17 troctolite 76535 (*25*). These ages are generally in the range suggested by CSFD from 4.26 Ga (*20*) to 4.31 Ga (*19*), making it the oldest impact basin on the Moon stratigraphically (*26*). As for the Apollo basin, CSFD measurements constrained its age to be 3.91 to 4.14 Ga (*19*, *20*), but it has not been constrained by any samples before CE-6.

CE-6 lunar sample composition

CE-6 sample CE6C0500YJFM002 was provided by CNSA for this research. Large fragments were extracted by handpicking. Nine clast mounts and six soil epoxy mounts were prepared from this sample. The mineralogy of all mounts was characterized by the TESCAN Integrated Mineral Analyzer (TIMA). TIMA has the advantage of investigating large numbers of particles simultaneously. The results, as the only ground truth, were compared with the in situ, remote sensing, and impact modeling results of SPA. These samples were scooped by a robotic arm at the surface (Fig. 2C), from a depth of ≤3 cm. The CE-6 sampling site is highly homogeneous (Fig. 2D), suggesting that the returned samples, although small in mass, could well represent the material of the landing site. In total, 1092 clasts ≥50 μm (fig. S6) and 2,935,175 soil particles ≥1 μm (fig. S7) were identified and analyzed.

The mineralogy of all mounts is similar (table S7). High-Ca pyroxene (HCP) and plagioclase (PLG) are the two most abundant minerals, with contents of 37.0 and 30.3 vol %, respectively. These two phases are predominantly from local basalts, the dominant material at the landing site. Ilmenite (ILM), olivine (OLV), Si-rich phase, and low-Ca pyroxene (LCP) also occur, with abundances of 3.8, 1.6, 1.1, and 0.2 vol %, respectively. Their mineralogy is shown in Fig. 6 (A and B). The clast mounts display a wider range, likely due to being controlled by large clasts. The soil results are uniform, similar to x-ray diffraction (XRD) results (*27*), both with lower PLG content than Raman results (*28*). The major element compositions of each mount (table S7) were computed on the basis of the modal abundance of constituent minerals and their elemental compositions. The average TiO_2, Al_2O_3, and FeO contents of all mounts are 2.3, 19.9, and

Downloaded from https://www.science.org on November 18, 2026

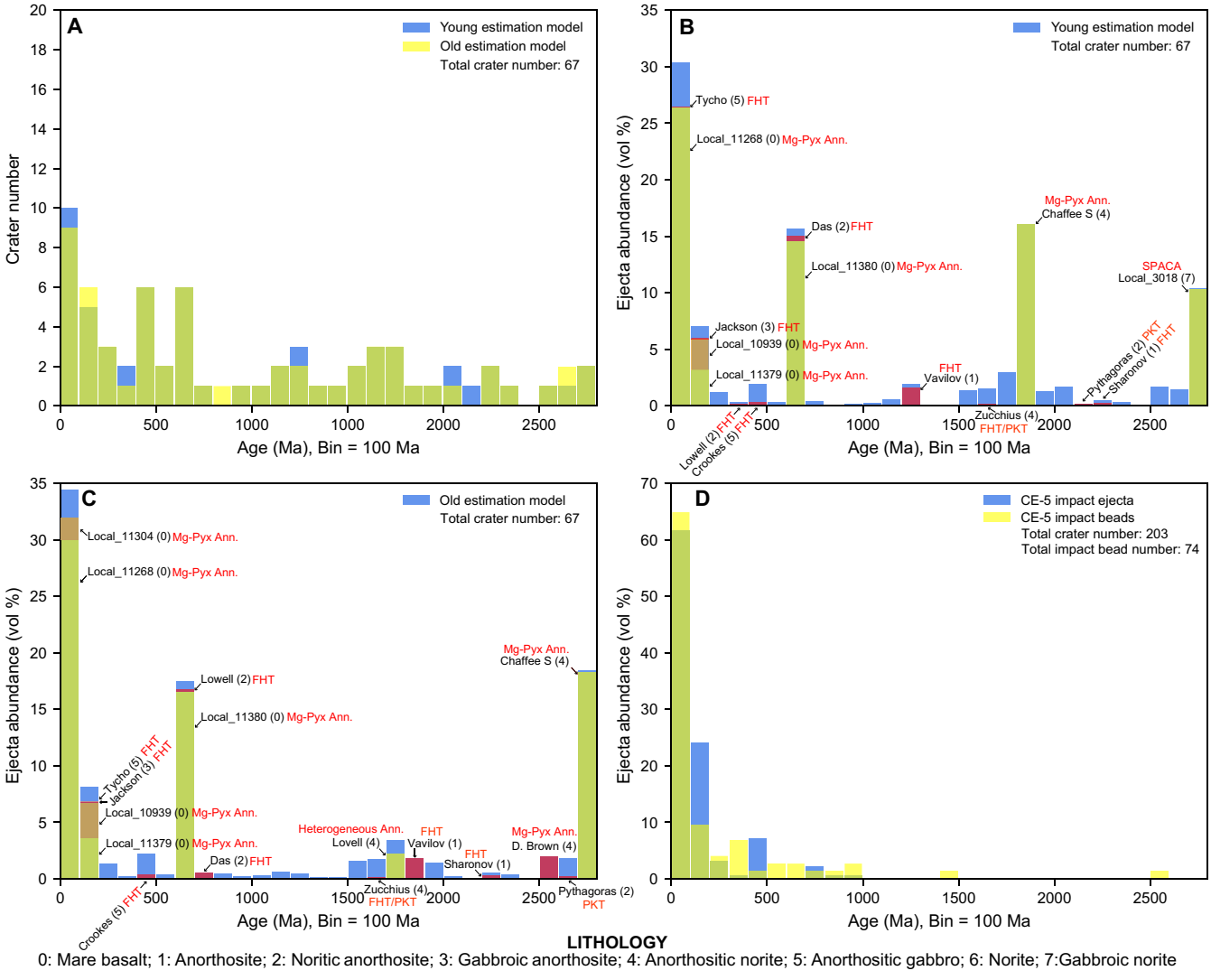

Fig. 5. Ages of source craters able to contribute >2 vol % of local mare material or >1 mm of nonmare material to the CE-6 site. (**A**) Number of craters in each age bin for both young and old estimates. (**B** and **C**) Ejecta abundance of each critical source crater for both the young and old estimates. Chaffee S is the most prominent distal crater that is able to deliver 16.1 to 18.2 vol % exotic materials. (**D**) Comparison with the source crater age distribution of the CE-5 site. CE-5 site (*17*) and returned samples (*65*) show one age peak younger than 500 Ma, but the CE-6 site shows more peaks, indicating a more complex impact history. The lithology is based on the mineral abundances obtained from Kaguya MI data (*30*, *31*).

15.4 wt %, respectively, and their average Mg# [Mg# = molar Mg/(Mg + Fe) * 100] is 33.7 (Fig. 6, C and D).

The contribution of each type of source crater was analyzed on the basis of the CE-6 soil compositions obtained here and in previous works (*27*–*29*) (Fig. 6, A to D). The mineralogical (*30*, *31*) and elemental (*32*) compositions of source craters (local maria, SPACA, MPA, HA, and FHT) were extracted from Kaguya Multiband Imager (MI) data. CE-6 soils have higher PLG contents than local mare source craters (Fig. 6, A and B), indicating the addition of nonmare materials. The concentrations of Al_2O_3 and FeO were used to constrain their contributions. A linear mixing model suggests an ~40 to 50 vol % addition of FHT/MPA into local basalts to produce CE-6 soils (orange and violet squares). It agrees with impact modeling results of ejecta source craters (red and blue circles; Fig. 6, C and D), suggesting <5 vol % feldspathic (from FHT) and ~35 to 45 vol % Mg-rich noritic components (mainly from Chaffee S on the Apollo western peak ring) were added.

PYX (41,695 in total) and PLG (16,150 in total) grain compositions were determined by TIMA. We plotted PYX Mg# and PLG An# [An# = molar Ca / (Ca + Na + K) * 100] in CE-6 soils in Fig. 6 (E and F), compared with those from the literature (2098 PYX and 1564 PLG grains, respectively; figs. S8 and S9 and table S8). The Mg# and An# distributions show two distinct peaks. The prominent peak (Mg# at ~62; An# at ~88) apparently represents PYX and PLG from local mare basalts (figs. S8 and S9). The second peak with higher Mg# (~84) and An# (~94) is most likely from the added Mg-rich noritic materials because the addition of feldspathic materials is minor (<5 vol %), and they have lower Mg# for PYX and higher An# for PLG (figs. S8 and S9). We plotted the PYX composition quadrilateral diagram of our PYX with PYX in Mg-suites (*33*), Apollo

Downloaded from https://www.science.org on November 18, 2026

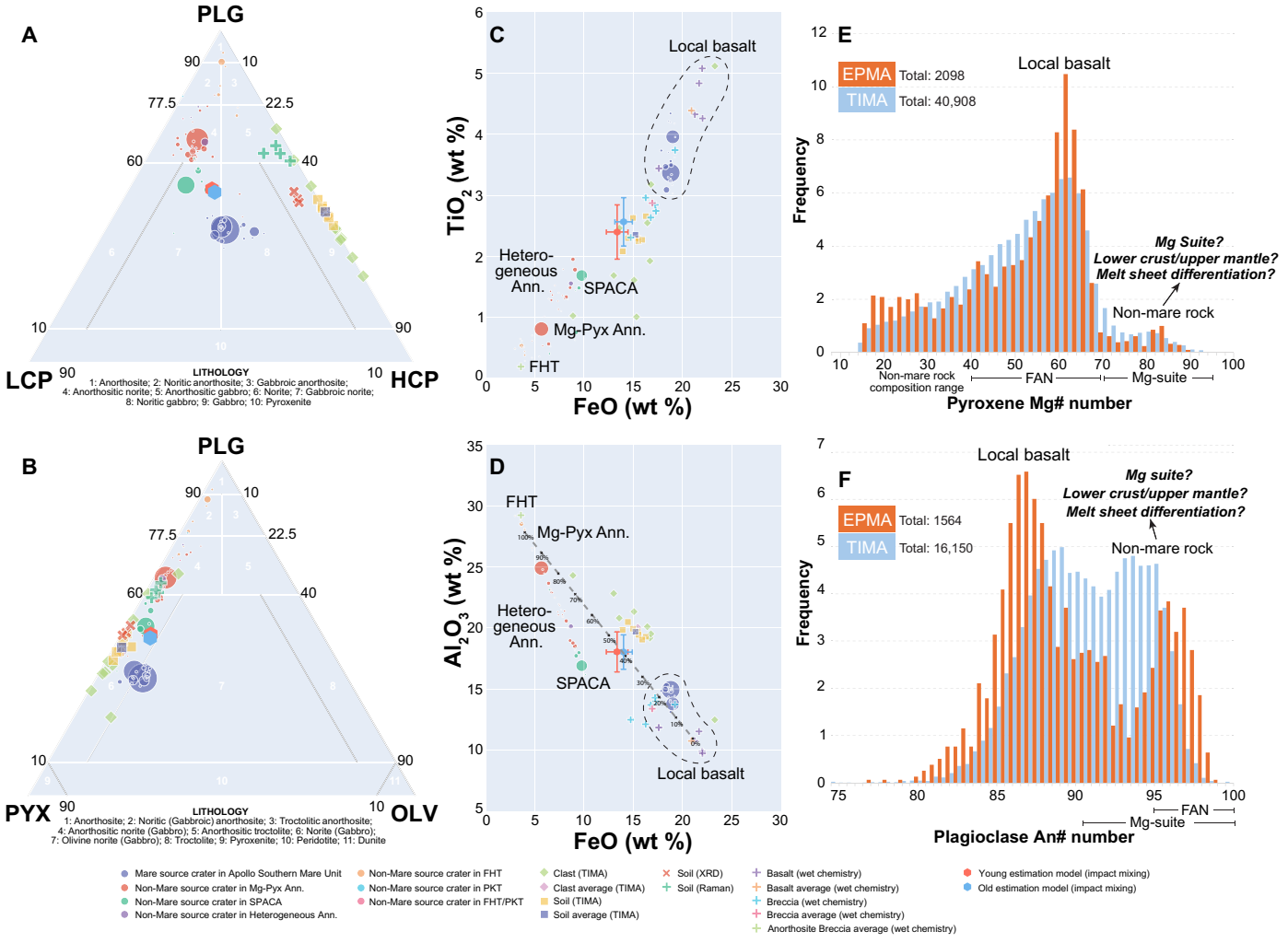

Fig. 6. Composition of CE-6 soils. (**A** and **B**) Mineralogy of the CE-6 soils, obtained by TIMA (this study), XRD (*27*), Raman (*28*), and predicted here using the ejecta model. (**C** and **D**) Major element abundances of CE-6 soils, basalts, breccias, and anorthosites, obtained by TIMA (this study), wet chemistry method (*29*), and predicted here using the ejecta model. The elemental and mineralogical compositions of the source crater are from Kaguya MI data. The diameter of each source crater circle represents its relative ejecta contribution. The CE-6 composition (orange and violet squares) indicates an ~40 to 50 vol % mixing between MPA and local basalts, consistent with the impact model (red and blue circles). (**E** and **F**) PYX Mg# and PLG An# of CE-6 soils. The Mg# and An# display two peaks. The prominent one (Mg# at ~62; An# at ~88) represents local basalt. The second peak with higher Mg# (~84) and An# (~94) is likely to be from added Mg-rich noritic materials. The lithology (*30*, *31*) and major element composition (*32*) are based on Kaguya MI data. CE-6 soil XRD and Raman data are from (*27*) and (*28*), respectively. CE-6 basalt, breccia, and anorthosite breccia wet chemistry data are from (*29*).

mission impactites, CE-6 noritic clasts (*34*), and local basalts (Fig. 7, E and F). This shows that the PYX investigated are mainly from local basalts with a Mg# value <74 (gray area, Fig. 7E). The remainder have compositions similar to the Mg-suite and Apollo mission impactites (Fig. 7E), with higher Mg contents (Mg# ≥ 74). Most high-Mg PYX and CE-6 noritic clasts (*34*) are located in the Mg-suite range.

CE-4 VNIS and CE-6 LMS mineralogy

CE-4 and CE-6 are the only two missions that have landed in SPA to date (Fig. 1A), carrying the Visible and Near-infrared Imaging Spectrometer (VNIS, 0.45 to 2.4 μm, onboard the CE-4 Yutu-2 rover; Fig. 2A) and the Lunar Mineralogical Spectrometer (LMS, 0.48 to 3.2 μm, onboard the CE-6 lander; Fig. 2C), respectively. CE-4 VNIS and CE-6 LMS data were used to constrain the landing site soil characteristics, which are likely mixed between local mare basalts and exotic materials. In this study, level 2B data were used after dark current, flat-field, temperature, radiometric, and geometric corrections (*35*, *36*). The irradiance spectra were converted to reflectance divided by solar irradiance. For CE-4 VNIS, 36 observations collected between 03 January 2019 and 05 April 2022 were used (fig. S10 and table S9). Among these, 30 spectra were obtained from soil targets (red dots, Figs. 2B) and 6 (CE4-D0015, D0107, D0150, D0168, D0177, and D0239) were obtained from rock targets (yellow dots, Fig. 2B). For CE-6 LMS, 14 spectra were collected in the all-band hyperspectral mode (fig. S11 and table S10). All of these are from soil targets. CE6-D0003 and D0017/D0022 of the sampling area were obtained before and after sampling (fig. S11).

On the basis of our impact modeling, the dominant nonmare components in CE-4 and CE-6 soils originate from Finsen and Chaffee S craters, respectively. Therefore, we extracted the spectra

Downloaded from https://www.science.org on November 18, 2026

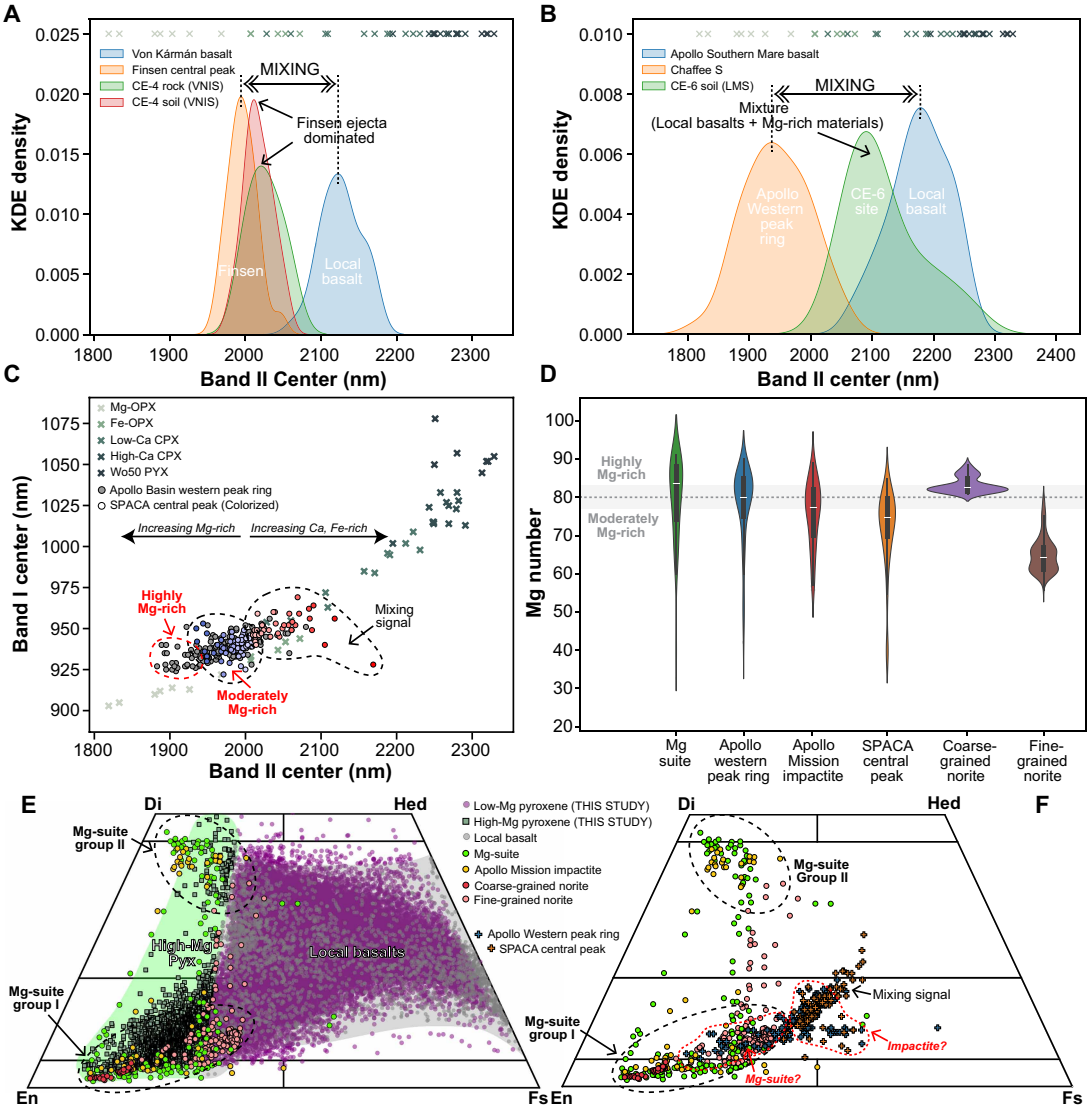

Fig. 7. Compositional comparison between CE-4/CE-6 soils, Apollo western peak ring, and SPACA central peaks. (**A**) BC2 of the CE-4 site (VNIS), local basalts, and Finsen central peak, indicating that CE-4 soil is dominated by Finsen ejecta. (**B**) BC2 of the CE-6 site (LMS), local basalts, and Chaffee S, indicating that the CE-6 soil is a mixture of local basalts and Chaffee S ejecta. (**C**) BC1/BC2 of the Apollo western peak ring, indicating that it is more Mg-rich than SPACA central peaks. (**D**) Mg# of Apollo western peak ring, comparable to Mg-suite and CE-6 coarse-grained norites, higher than impactites, fine-grained norites, and SPACA central peaks. Mg# of Mg-suite, Apollo mission impactites, coarse-grained norites, and fine-grained norites are constrained by samples (fig. S8). Mg# of Apollo western peak ring and SPACA central peaks are constrained by M^3 data here (table S11). Mg-suite, Apollo western peak ring, and coarse-grained norite are mainly highly Mg-rich. The rest are moderately Mg-rich. (**E** and **F**) PYX composition of the CE-6 soils (TIMA), local basalts/norites/impactite (EPMA; fig. S8), and the Apollo western peak ring and SPACA central peaks (M^3). Moderately (SPACA central peaks) and highly Mg-rich materials (Apollo western peak ring) are closest to impactites and the Mg-suite, respectively.

of these two craters based on Moon Mineralogy Mapper (M^3) data (0.43 to 3.0 μm) to evaluate the relative degree of mixing (fig. S12). The spectra of pristine basalts were obtained from small fresh craters in Von Kármán crater and the southern Apollo basin. All of the spectra were processed using the procedure in (*37*) to obtain their spectral indices (Band I and II centers; BC1 and BC2), together with typical lunar minerals (Mg-OPX, Fe-OPX, low-Ca CPX, high-Ca CPX, Wo50-PYX) (*38*) for comparison (see Materials and Methods). After KDE density analysis, we found that both BC2 of CE-4 soil (~2011 nm) and surface rocks (~2020 nm) are very close to that of the Finsen central peak (~1994 nm) but distinct from local mare basalts on the floor of Von Kármán (~2,123 nm) (Fig. 7A). The first three have a PYX composition closer to Mg-OPX and Fe-OPX, which might be moderately Mg-rich noritic materials, and the last one shows a PYX composition of low-Ca CPX, typical for mare basalts (*38*). This indicates that the CE-4 surface materials are predominantly from Finsen ejecta, with little contamination from local basalts by lateral or vertical mixing. For the CE-6 soil, the BC2 is ~2090 nm (Fe-OPX to low-Ca CPX), closer to local basalts at ~2180 nm (low-Ca CPX to high-Ca CPX), but far away from that of Chaffee S at ~1935 nm (Mg-OPX) (Fig. 7B). It suggests that more materials are from local basalts at the CE-6 site than CE-4, but there are still considerable amounts of nonmare materials at the CE-6 site, similar to our predictions by impact modeling (~40

Downloaded from https://www.science.org on November 18, 2026

to 50 vol %). For both sites, the added nonmare materials are Mg-rich with a BC2 of <2000 nm; it is even more highly Mg-rich for Chaffee S (located at the Apollo western peak ring) than Finsen, with shorter BC2 absorptions.

SPA basin mineralogy

The spectra of SPA were comprehensively investigated to constrain the nature of nonmare materials at the CE-4 and CE-6 sites. M^3 OP2C1 and OP2C2 data were mosaicked for the entire SPA to assess its spectral features (see Materials and Methods), as shown in Fig. 8 (A and B). The boundaries of SPA compositional zones (*5*) generally match the BC2 of the basin. From the center to the exterior, it is characterized by intermediate-Ca, Fe pyroxenes (SPACA, >2000 nm) and Mg-rich pyroxenes (MPA, <2000 nm) (*38*). Many complex crater central peaks in SPACA show Mg-rich compositions (BC2 <2000 nm), such as Bhabha, Stoney, and Finsen (Fig. S13, E to G), indicating the presence of underearth moderately Mg-rich materials, as central peak excavate the deepest materials of a complex crater (*39*). White crater, the closest complex crater to CE-6 within SPACA (Fig. 8B), does not display Mg-rich signatures (BC2 >2000 nm) at its central peak (Fig. S13H). All the continuous ejecta deposits of these four central peak craters are characterized by long-wavelength BC2 (>2100 nm; Fig. S13, E to H), indicating that the upper layers are basaltic in composition. In addition, the Apollo western peak ring, where most of the nonmare materials in CE-6 samples originated from, reveals a much more Mg-rich nature (deep purple in Fig. 8B) compared to SPACA central peaks and all other adjacent materials. Other parts of the Apollo peak ring display moderately Mg-rich signals, but their distribution is limited. Apollo basin is the only impact basin in SPA that has exposed such large amounts of highly Mg-rich materials on its western peak ring (Fig. 8B).

In addition, individual spectra were extracted from small fresh craters on the Apollo western peak ring and SPACA central peaks (Bhabha, Stoney, Finsen, and White) (fig. S12 and table S11) from M^3 OP2C1/OP2C2 data to mitigate space weathering effects. We computed the absorption features, PYX compositions (*40*), and Mg# of each spectrum (text S3 and fig. S14). BC1 and BC2 of the Apollo western peak ring and SPACA central peaks are plotted in Fig. 7C and shown in Fig. 8 (C to G). Those with BC2 >2000 nm are mainly located on the boundary of the units investigated and surrounding materials and are thus likely to be contaminated spectra. As discussed above, compared to other SPACA complex craters, the central peak of White is not Mg-rich with BC2 >2000 nm (Fig. 8G). BC2 (<1950 nm; comparable to Mg-OPX in composition) of the Apollo western peak ring is much shorter than SPACA central peaks (Fig. 8C), indicating that the Apollo basin excavates much more Mg-rich materials than complex craters in SPACA. This is also reflected by the computed Mg# of the Apollo western peak ring and SPACA central peaks based on M^3 (Fig. 7D). The Apollo basin western peak ring has significantly higher Mg# than SPACA central peaks, comparable to those in the Mg-suite, Apollo mission impactites, covering the range of CE-6 noritic clasts (Fig. 7D and fig. S8) (*34*). In addition, the PYX compositions were estimated by the method in (*40*) and plotted together with Mg-suite, Apollo mission impactites, and CE-6 noritic clasts. This indicates that the Apollo western peak ring has distinctive PYX compositions compared to SPACA central peaks, more similar to Mg-suite group I, Apollo mission impactites, and CE-6 coarse-grained noritic clasts, but SPACA central peaks are closer to CE-6 fine-grained noritic clasts (*34*).

DISCUSSION

Moderately and highly Mg-rich materials in the SPA basin

As discussed above, moderately and highly Mg-rich materials were widely distributed in the SPA basin, mainly at the SPACA central peak and Apollo western peak ring (Fig. 8, A and B), which have been investigated in situ by the CE-4 and CE-6 missions, respectively. They have different mineralogy and compositions (Fig. 7, C to F), indicating their distinct formation mechanisms.

The highly Mg-rich materials, delivered to the CE-6 site by Chaffee S crater (~15.0 cm of primary ejecta) from the Apollo western peak ring, are likely to be products of Mg-suite magmatism in SPA. They are much more Mg-rich than the SPACA central peaks (shorter BC2 and higher Mg#; Fig. 7, C and D), with lower Th abundance [<2 parts per million (ppm); Fig. 4A], consistent with the composition of the KREEP-poor Mg-suite (*41*). An increasing number of KREEP-poor Mg-suite samples have been found recently (e.g., Dhofar 489, NWA 10401, and Arguin 002), including Arguin 002, which has been interpreted from SPA, supporting that the KREEP-poor Mg-suite magmatism existed in the basin (*42*). The Mg-suite origin of highly Mg-rich materials is also supported by their mineralogy constrained by orbital spectra data and the CE-6 samples. Both the PYX compositions of the Apollo western peak ring (Fig. 7F) and the high-Mg PYX in the CE-6 samples (Fig. 7E) are in the compositional range of the Mg-suite (*33*). In addition, by compiling the outcrops of Mg-rich and anorthosite in the Apollo basin from M^3 hyperspectral and multispectral MI data (Fig. 8, A to C) (*43*, *44*), it was found that they coexist in the Apollo basin peak ring, which indicates the intrusion of Mg-rich materials into the anorthosite crust that were later exposed by the Apollo impact concurrently.

Surface morphologies and gravity data further suggest a Mg-suite origin for the highly Mg-rich materials on Apollo western peak ring. As the largest impact basin, SPA thinned its crust to a range (25 to 35 km; fig. S15) (*45*), where intrusions are favored and present as floor-modified craters (FMCs) (*46*). These craters include Oppenheimer and two less well-developed FMCs (Apollo X and Q; see text S4) on the western, northwestern, and southwestern rims of Apollo (Fig. 8, A and B). Among them, Apollo Q is the most ancient, predating the Apollo impact, with its northeastern rim destroyed by Apollo (fig. S16, C and D). Apollo X and Oppenheimer are younger than Apollo and crosscut its rim (Fig. S16, A and B). The distribution of subsurface intrusions reflected by FMCs that both predate and postdate the Apollo basin indicates that intrusive magmatism existed in this region at the time of Apollo impact. In addition, on the basis of the GRAIL gravity data, 14 dikes were identified under the Apollo basin, with a total length of >2200 km, root and roof depths of ~37 to 49 km and <4 to 9 km, making it the most extensive intrusive system on the farside (*47*). Such a burial depth is consistent with the formation depth of most Mg-suites with plutonic or hypabyssal features (<20 km) (*33*), including Arguin 002 (12 to 20 km), potentially from SPA (*42*). The Apollo impact, with an excavation depth down to 30 km (*48*), could excavate these the highly Mg-rich materials into the basin materials.

As for the moderately Mg-rich materials mainly exposed at SPACA central peaks, their spectra indicate that their Mg# is lower than that of the Mg-suite (*33*) (Fig. 7D), with different PYX compositions (Fig. 7F). Their composition is closer to Apollo mission impactites, indicating that an impact origin is more plausible (Fig. 7, D and F). Therefore, this study supports the hypothesis that the Mg-rich materials at the SPACA central peaks originated from SPA melt sheet differentiation

Downloaded from https://www.science.org on November 18, 2026

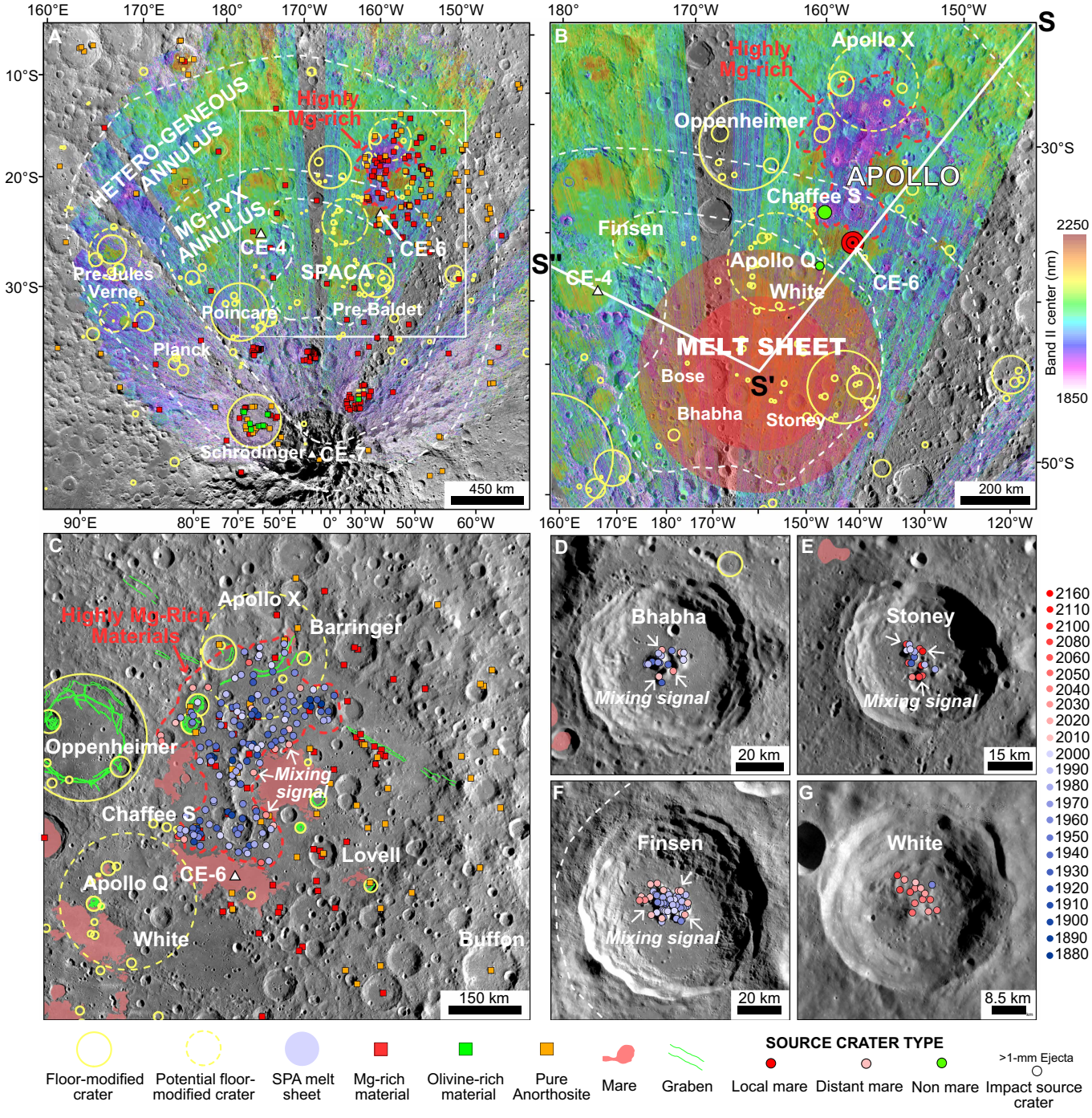

Fig. 8. Moderately and highly Mg-rich materials in SPA. (**A**) FMCs and Mg-rich materials (BC2 <2000 nm) in SPA. The occurrence of pure anorthosite (PAN) indicates the preservation of crustal materials. The outcrops of olivine-rich, Mg-rich, and PAN are summarized from (*18*, *43*, *44*). (**B**) Major impact source craters surrounding the CE-6 site and the suggested SPA melt sheet [red circles, with diameters of 400 or 630 km (*12*)]. The white thick line (S-S′-S″) represents the profile line for Fig. 9A. (**C** to **G**) M^3 BC2 of the highly Mg-rich Apollo western peak ring, and moderately Mg-rich SPACA central peaks (Bhabha, Stoney, and Finsen). The central peak of White crater shows basaltic signatures. Apollo basin and White crater are located at the edge of the proposed SPA melt sheet.

Downloaded from https://www.science.org on November 18, 2026

(*12*) rather than Mg-rich magmatism. A lower crust/upper mantle origin is not preferred because of many impact features in SPACA with deeper excavation depth that do not display Mg-rich signatures (e.g., Pre-Baldet crater; Fig. 8, A and B). It is noted that some moderately Mg-rich materials are exposed on the Apollo western peak ring, which cannot be distinguished from that of the SPACA central peak (Fig. 7, C and D). The central peak of White crater, the closest complex crater on the southwestern rim of the Apollo basin (Fig. 8C), does not show a Mg-rich composition (Fig. 8G and fig. S13H). Its excavation depth could readily reach the proposed Mg-rich layer of the SPA melt sheet (6.0 km), if exists, but it is not exposed. This may be because it is at the boundary of the melt sheet (Fig. 8B) (*12*), where it is not thick enough for differentiation. Therefore, the moderately Mg-rich materials of the Apollo western peak ring are unlikely to represent differentiation products but rather a mixture of Mg-suite and crustal materials, similar to other parts of the Apollo peak ring (Fig. 8B).

This study presented the ground truth of moderately and highly Mg-rich materials in the SPA basin by the CE-4 and CE-6 missions from two locations in SPA, i.e., Von Kármán crater and Apollo basin. However, it might be subject to the representativeness of in situ data and collected samples from a localized region, and the different working scales when comparing samples, in situ VNIS/LMS, and orbital remote sensing measurements. This issue might be subdued because CE-4 and CE-6 landed on mare units and their landing sites are homogeneous at least in intermediate (in meters) to large scales (in kilometers; Fig. 2). More missions to the SPA basin, such as the CE-7 and Artemis IV missions to the south pole, and the Endurance mission across SPA, would provide additional ground truth from multiple locations of SPA where Mg-rich materials are expected to be present (Fig. 8A). They will finally provide in situ data and samples at multiple scales and areas, together to examine the origin of Mg-rich lithologies of SPA and construct a more complete postimpact evolution history of SPA (*6*).

Major impact events in the SPA basin

Nonmare clasts were used to date major impact events recorded by CE-6 samples (*34*, *49*, *50*). The noritic clasts are the dominant nonmare components (>90%) in the samples (see Results). We also found numerous PYX grains likely from these norites with similar compositions (Fig. 7E). They were classified into coarse-grained (mean Mg# = 83) and fine-grained (mean Mg# = 65) norites in (*34*) (Fig. 7D). Su *et al.* (*34*) proposed that the fine-grained noritic clasts were originated from the differentiation of the SPA melt sheet but the coarse-grained ones more controversial with plutonic textures and composition similar to Mg-suite (*34*).

An age has been reported for the coarse-grained norite (4245 ± 2 Ma) (*34*), the same as the Pb-Pb chronology of CE-6 impact melt rocks (4245 ± 4 Ma) (*50*). On the basis of the dominance of norites in the nonmare fraction of the CE-6 samples, they are highly likely derived directly from the critical source craters listed in Table 1, not from less efficient lateral diffusion. Therefore, Chaffee S on the Apollo western peak ring, which contributed ~35 to 50 vol % ejecta among all nonmare components, is the most probable source. In this case, we propose that the coarse-grained norites likely correspond to the highly Mg-rich materials exposed on the Apollo western peak ring (Fig. 8B). They are likely to be products of Mg-suite magmatism and therefore develop plutonic textures (*34*). The protolith of these highly Mg-rich materials is likely to be KREEP-poor Mg-suite, similar to Arguin 002 (*42*). They intruded into the Apollo basin crust before the impact, and their isotopic ages were reset by Apollo to ~4.25 Ga and then later delivered to the CE-6 site by the Chaffee S impact. Besides, many of the Mg-suite materials from the Apollo western peak ring might stay pristine, such as the Mg-suite fragments in the CE-6 samples (*34*, *51*) with an age of 4340 ± 4 Ma. It is indistinguishable from the age of Arguin 002 (4342 ± 93 Ma), potentially from SPA (*42*), indicating Mg-suite plutonism occurring in SPA at ~4.34 Ga. In summary, the age of ~4.25 Ga is unlikely to represent the age of SPA but rather that of the Apollo impact. Recently, Chen *et al.* (*49*) reported ages of 4164 ± 7 Ma and 4184 ± 40 Ma for two CE-6 impact melt clasts with a composition similar to Apollo 15 gabbro/QMD, suggesting they represent the Apollo impact time. This possibility still exists because gabbro/QMDs are more evolved than Mg-suite, perhaps from large-degree fractionation from the same parent magma as Mg-suite (*52*) or remelting of the SPA melt sheet by the Apollo impact (*12*); both of them were found in this region (Fig. 8B). In any case, the Apollo impact occurred at ~4.2 Ga. Thus, SPA must have formed before ~4.25 Ga, and the widely proposed SPA age at 4.34 Ga (*23*, *24*) appears to be the best candidate, especially given that one CE-6 impact melt rock has a $^{40}Ar/^{39}Ar$ age of 4330 ± 65 Ma (*53*). If SPA formed younger at 4.25 Ga (*25*, *34*), it is inconsistent with our constraints, and it will be challenging to explain the age of the 4.34-Ga Mg-suite magmatism in SPA (*34*, *42*) that is not reset by the SPA impact itself, which has a global effect (*3*). Even if it were, the age discrepancy between the SPA and Apollo basins was too short to form all the other basins within SPA (*1*, *19*), making it less likely.

As for the fine-grained norites in the CE-6 samples, they show a variation in ages from 4200 ± 7 to 4254 ± 14 Ma (mean = 4227 ± 20 Ma), and from 3841 ± 23 to 3903 ± 6 Ma (mean = 3869 ± 16 Ma) (*34*). The 3.87-Ga age was also found in the CE-6 impact melt rocks (3876 ± 4 Ma) (*50*), indicating that it records a major impact event at the CE-6 site. Their PYX compositions are similar to the Apollo mission impactites (Fig. 7, D and E, and fig. S8), as well as the SPACA central peaks (Fig. 7F). Therefore, these fine-grained norites most likely represent impactites, and at least two episodes of impact events were recorded by these samples. The older cluster with ages concentrated at 4227 ± 20 Ma shows a spectrum of ages, many of them statistically distinct. They could be well explained by the thick melt sheet differentiation, either from the older SPA impact (the extraction of KREEP elements to the melt sheet (*9*) and tidal heating (*54*) could dramatically delay the solidification age) or the younger Apollo impact. More detailed thermodynamic models need to be conducted to assess these two hypotheses. Impact source craters do exist in the SPA melt sheet and Apollo basin (Figs. 3B and 8B) that are able to transport these materials to the CE-6 site.

Su *et al.* (*34*) proposed that the 3.87 Ga age represents the age of the Apollo impact, but this conflicts with our discussions above. This extremely young age for Apollo is younger than all CSFD estimates (3.91 to 4.14 Ga) for this basin (*19*, *20*). According to our impact modeling, we propose that 3.87 Ga most likely represents the age of Orientale, close to its CSFD model ages between 3.80 and 3.81 Ga (*19*, *22*). Orientale has the largest primary ejecta thickness (~29.3 m; Table 1 and fig. S6) in this region, overlying all other basin materials, including Apollo and SPA (Fig. 9B). It is more likely to sample its basin materials than all the other underlying older basins. Although the Schrödinger basin might have a similar age, its ejecta (~0.4 m of primary ejecta; table S6) is negligible compared to Orientale, making the 3.87-Ga age less likely to represent

Downloaded from https://www.science.org on November 18, 2026

Schrödinger. The ejecta of Orientale are now exposed at the surface of Cryptomare White-Grissom and buried under subsequent basalts in the Apollo basin (Fig. 9B) (*8*). After Orientale, Imbrium basin is the second-largest contributor (~22.5 m of primary ejecta) of basin materials, apart from Apollo and SPA. Therefore, its materials might also be acquired by CE-6. Located within PKT, these potential Imbrium materials might have an elevated KREEP abundance (>4 ppm Th), compared to the slightly KREEP-rich (2 to 4 ppm Th) SPA materials, and KREEP-poor (<2 ppm Th) FHT materials (*55*). Lots of fragments were found to be KREEP-rich from the CE-6 samples, including impact glass beads (*56*, *57*) and lithic fragments (*58*). Although they have not been dated so far, some of them might have originated from the Imbrium basin because of their KREEP affinity, and it needs to pay attention to the impactites with an age of ~3.92 Ga (*21*) from the CE-6 samples in the future sample studies.

Geological evolution of the SPA basin

All in all, this study constrained the sequence of critical geological events in SPA and constructed the postimpact geological evolution history of this Moon's largest impact basin below and illustrated in Fig. 9. The SPA impact occurred at ~4.34 Ga (*23*, *24*), creating a 2050 km–by–2400 km–diameter basin cavity and a massive melt sheet (*12*). The tremendous energy released might have triggered mantle overturn (*3*), induced global magmatism (*24*), including KREEP-poor Mg-suite in SPA (*59*), now exposed at the Apollo western peak ring (Fig. 8B). The differentiation of SPA melt sheet at SPACA created a thick moderately Mg-rich noritic layer, overlapped by a basaltic layer (*12*) probably from melt sheet differentiation as well (*5*) or cryptomare volcanism at ~4.20 Ga (*11*). Together with the MPA, likely to be excavated deep materials, and the HA as a transitional zone, it formed the compositional architecture of the SPA crust (SPACA-MPA-HA-SPA exterior; Fig. 1, A to C) (*5*).

In the Pre-Nectarian period, numbers of impact features formed within and outside SPA, including Australe North, Smythii (4.26 Ga) (*19*), and Apollo Q. At ~4.2 Ga, a projectile struck the northeastern SPA basin, forming the largest basin within SPA, the Apollo basin (*48*). Another projectile impacted the northwestern SPA at a similar time (~4.2 Ga) (*16*), creating the Von Kármán crater. The Apollo impact excavated previously intruded highly Mg-rich Mg-suite rocks on its western peak ring (Fig. 8B), reset their ages, and destroyed the northeastern rim of Apollo Q (fig. S16CD). After the Apollo impact, Mendel-Rydberg (4.13 Ga) (*19*), Crisium (4.07 Ga) (*19*), Oppenheimer (4.04 Ga) (*20*), Imbrium (3.92 Ga) (*21*), and Orientale (3.87 Ga) basins formed (Table 1). All the above basin materials were buried by Orientale ejecta. Apollo X formed on the northwestern rim of Apollo in the Pre-Nectarian period, followed by Oppenheimer in the Nectarian Period (*60*). These impact events will not only deliver primary ejecta to the CE-6 site, but their ballistic deposition would excavate and redistribute preexisting materials and mix with them (*15*), forming the total ejecta with substantial amount of preexisting components (Fig. 9B). It will make the inferred stratigraphy more heterogeneous and diffused but, in principle, is still able to indicate the major basin sources at the CE-6 site. Orientale and Imbrium are the two largest distant basin material contributors, with primary ejecta thicknesses of 29.3 and 22.5 m, penetrating through local materials down to 270 and 384 m (Table 1). They will be mixed with older basin materials (such as Oppenheimer, Crisium, Mendel-Rydberg, Apollo, and SPA basins) and finally delivered to the CE-6 site by later impact transportation.

Immediately after the formation of SPA up to at least the Nectarian period (*61*), intrusive magmatism was extensive in SPA, forming numbers of FMCs (e.g., Oppenheimer, Apollo Q, and X) and magmatic dikes with or without Mg-rich compositions. At the Apollo basin, linear dikes have a total length of ~2200 km and a volume of ~1.2×10^4 km^3, 15 times the volume of the effusive basalts (*47*). Major complex craters formed within SPACA from the Nectarian to the Imbrian period, including Stoney (3.86 Ga), Bose (3.82 Ga), Bhabha (3.81 Ga) (*60*), and Finsen (3.1 Ga) (*16*), exposing moderately Mg-rich materials on their central peaks (fig. S13, E to G), which differentiated from the SPA melt sheet (*12*).

From the Nectarian to the Eratosthenian periods, effusive volcanism was active in SPA (*8*). The mare basalts (>4.0 Ga) to the south of Apollo basin were covered by the ejecta of Orientale to form Cryptomare White-Grissom (Fig. 3B) (*8*). At Von Kármán crater, mare basalts erupted on its floor at ~3.6 Ga (*7*) but were later buried by Finsen ejecta in the northeastern part at ~3.1 Ga (Fig. 1D) (*16*). CE-4 landed on Finsen continuous ejecta and is currently investigating moderately Mg-rich SPA melt sheet differentiation products at SPACA. At the Apollo basin, mare basalts erupted in six episodes (*8*). The southern Apollo basin has experienced two stages of eruptions, and CE-6 landed on the ~2.83-Ga low-Ti basalts (*10*, *11*), overlying 2.93-Ga very low-Ti basalts (*62*).

Following mare eruptions, the CE-6 site accumulated diverse exotic materials from SPA and beyond (Table 1 and table S4). At 1.84/2.79 Ga (*63*, *64*), Chaffee S formed on the Apollo western peak ring, contributing ~15.0 cm of highly Mg-rich ejecta to the CE-6 site, dominating nonmare fractions in the samples (~35 to 50 vol %), together with Local_3018 (2.8 of 3.4 Ga), Lovell (1.75 Ga), D. Brown (2.54 Ga) that contributed 2 vol % of moderately Mg-rich materials, and Vavilov (1.26/1.86 Ga), Crookes (488 Ma), Sharonov (2.2 Ga), Lowell (374/652 Ma), Jackson (147 Ma), and Tycho (58 and 124 Ma) craters that delivered ≥0.1 cm of anorthositic materials.

In the Copernican period, small local impacts <5 km in distance dominated, reflecting the recent inner Solar System dynamics (*65*), similar to the CE-5 site (Fig. 5D). A study of the age of impact melt beads in CE-6 samples will shed light on the recent impact history of the farside to establish a global picture of lunar impact cratering.

MATERIALS AND METHODS

Impact source crater database

Impact source crater catalog

We used the ejecta decay model of Sharpton (*13*) and Pike (*14*) to calculate the ejecta thickness of impact craters (simple and complex craters) and impact basins, respectively, both calibrated to the lunar observation data. A catalog including all candidate source craters globally that are able to contribute nonnegligible ejecta to the CE-6 site was constructed. The ejecta from all impact basins were not included because even the youngest Orientale basin (~3.87 Ga) formed before the CE-6 local basalts at ~2.83 Ga (*10*, *11*). The ejecta thickness of all craters was estimated by Sharpton's model (*13*). For simple craters, $\delta = 0.014R^{1.01}(r/R)^{-3}$; for complex craters, $\delta = 3.95R^{0.399}(r/R)^{-3}$, where δ represents primary ejecta thickness (in meters), R is the crater radius (in meters), and r is the radial distance (in meters) from the crater center to the landing site. Besides, during the ballistic deposition of primary ejecta, they will excavate, redistribute, and mix with local materials, and their sum becomes the total ejecta. The mixing ratio (μ′) could be estimated by the following

Downloaded from https://www.science.org on November 18, 2026

equations: $\mu' = \mu$ ($\mu \leq 5$), $\mu' = \mu/2 + 2.5$ ($\mu > 5$), and $\mu = 0.0183r^{0.87}$ (in kilometers) (*15*). We subdivided areas surrounding the CE-6 landing site into distance range of [0 to 50) m, [50 to 250) m, [250 to 500) m, [0.5 to 1) km, [1 to 2) km, [2 to 4) km, [4 to 8) km, [8 to 16) km, [16 to 32) km, [32 to 64) km, [64 to 128) km, [128 to 256) km, [128 to 256) km, [256 to 512) km, and ≥512 km, and computed the crater radius that was able to deliver 1 cm of primary ejecta (except for <50 m, ≥512 km) for the starting distance of each range. This ensures that all craters that contribute ≥1 cm of ejecta in each range are included. These values were rounded down to include even more candidate sources (table S1); then, all craters larger than the rounded value were selected on the basis of the CE-6 LCAM, LROC NAC, and TC Morning Map images. For distance range <50 m, all craters were included because any of them might deliver significant amounts of ejecta. A total of 11,378 craters <512 km were identified and labeled from "Local_0" to "Local_11377." For ≥512 km, the ejecta thickness

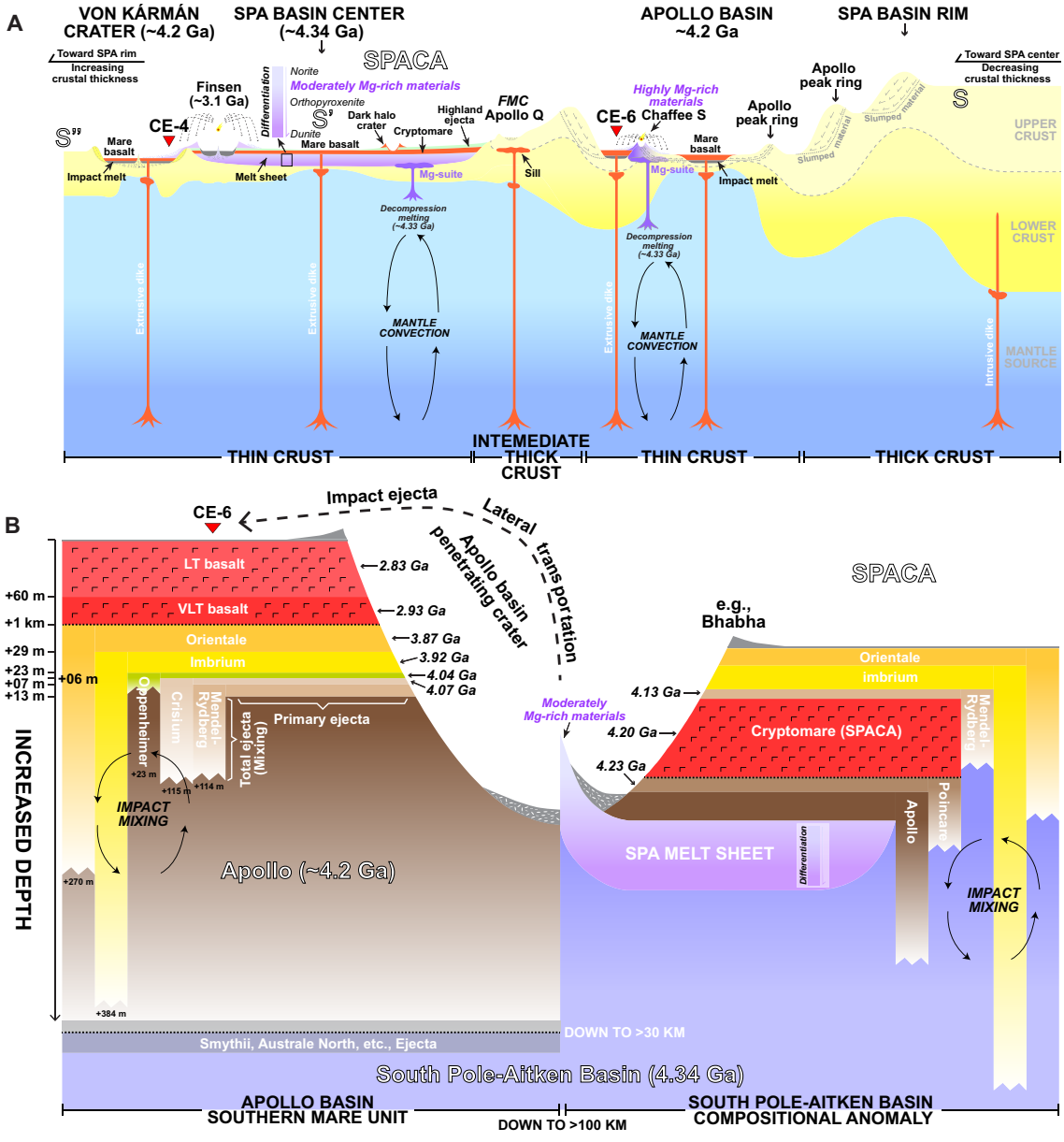

Fig. 9. Geological history of the SPA basin. (**A**) Geological section of the SPA basin. SPA melt sheet differentiation might produce moderately Mg-rich materials, now exposed at SPACA central peaks and delivered to the CE-4 site by the Finsen crater. Mg-suite magmatism is widespread in SPA and might produce highly Mg-rich materials. They are exposed at the Apollo western peak ring and were delivered to the CE-6 site by the Chaffee S crater. (**B**) Sequence of major impact basin events and their ejecta thickness in SPA. Orientale is the youngest impact basin whose ejecta (~29.3 m of primary ejecta) covered all older basin materials, including Apollo (~4.2 Ga) and SPA (~4.34 Ga). Impact basin events will not only deliver primary ejecta (horizontal rectangle), but their ballistic deposition would also excavate and redistribute preexisting materials (vertical rectangle) and mix with them. Orientale and Imbrium basin ejecta would excavate local materials down to 270 and 384 m, respectively, and mix them with older basin materials (such as Oppenheimer, Crisium, Mendel-Rydberg, Apollo, and SPA basins) as total ejecta. They might be transported to the CE-6 site by younger penetrating craters.

Downloaded from https://www.science.org on November 18, 2026

of all craters identified in (*2*) (nearly complete for craters ≥1 km, 1.26 million in total, labeled from "Distant_0" to "Distant_1267768") was calculated, and only those providing ≥1 cm of ejecta were included. Because of the >1 million craters investigated, we arbitrarily treated craters <18.8 and ≥18.8 km as simple and complex craters, respectively, based on the global simple-complex crater transition diameter (*66*). In total, 1836 impact craters were identified globally that were able to offer nonnegligible ejecta (≥0.1 cm) and were further studied (table S2 and fig. S1). This threshold (0.1 cm) is able to capture nearly all ejecta provenance information at the CE-6 site, far better than necessary, as only ~15 impact craters are able to contribute 1 vol % of primary ejecta (at least ~1 cm of ejecta is needed) (see below). Because of the curvature of the lunar globe, a spherical correction was applied to the ejecta thickness model of impact basins (not applied to impact craters because most of the impact craters able to contribute nonnegligible ejecta to the CE-6 site are very close to it). On a planar surface, the ejecta thickness of an impact basin could be estimated by the decay relationship of $\delta = 0.033R_t(r/R_t)^{-3.0}$ (δ represents primary ejecta thickness, r represents radial distance, and R_t represents transient cavity radius) (*14*). To correct the curvature of the Moon, we multiplied the original planar thickness by the ratio of the theoretical planar circumference to the actual spherical circumference, which yielded a corrected function for impact basin ejecta thickness $\delta = \left[0.033R\left(\frac{r}{R_t}\right)^{-3}\right]\left[\frac{r}{R_{Moon}Sin\left(\frac{r}{R_{Moon}}\right)}\right]$, where R_{Moon} represents the radius of the Moon. Besides, some ejecta from early basin-forming impacts may enter geocentric orbits and return to the Moon as sesquinary impacts in addition to ballistic ejecta. They are not included in our model, which might cause minor uncertainty, but most impact basin ejecta should be deposited ballistically.

Impact source crater age

Many of the selected source craters might have formed before the CE-6 basalts, with their ejecta buried; therefore, their ages were all constrained to locate postmare craters. We first determined their stratigraphic ages based on previous geological maps or their superposition relationship with adjacent geological units (*60*, *61*). Only Copernican- and Eratosthenian-aged craters (90 in total) were further analyzed to obtain their absolute ages (table S2); Imbrian-aged or older craters were unlikely to contribute ejecta directly. For these young craters, the ages of well-studied examples (e.g., Pythagoras, Tsiolkovskiy, and Vavilov) were taken from the literature (table S3) (*67*, *68*). All the rest were determined by the CSFD, or the CDM (text S1) and CMM (text S2), following the procedure in (*17*). CSFD measurements were conducted on the continuous ejecta of craters ≥1 km based on the LROC WAC images, TC Ortho Maps, or CE-2 CCD DOMs (fig. S2). CSFD curves were fitted by Craterstats2, using the production function in (*69*) and the chronology function in (*70*) (fig. S3). CDM and CMM were applied to smaller craters <1 km based on the CE-6 LCAM or LROC NAC data. CDM modeling was based on the crater degradation equation in (*71*, *72*). Crater Degradation Model 1 in (*17*) was used to constrain their ages (fig. S4). CMM modeling was based on the relationship between small crater morphology classes (A/AB/B/BC/C) and their residence time on the surface (*73*). On the basis of their morphology class and diameter, the lower/upper limit age of each crater was determined (fig. S5). In total, 67 craters were found to postdate local maria and were further studied for their contribution to the CE-6 site (Figs. 3 and 4). CDM and CMM results show good consistency and are validated by the Apollo mission and CE-5 results (text S2). Both the young and old estimates of their ages were considered to represent the age uncertainties, as young and old estimation models, respectively (table S3).

Impact source crater composition

To better understand the provenance of different components in the CE-6 soils, the characteristics of impact targets were constrained (table S4). First, they were classified into the Apollo southern mare unit, Nectarian crater unit, Nectarian terra unit, pre-Nectarian terra unit, light plain, Apollo basin peak ring, Apollo basin rim, etc., according to previous geological maps (*60*, *61*). Then, these targets were placed into the crustal terranes (SPA Terrane, FHT, and PKT). If located in SPA, they were subdivided into SPACA, MPA, and HA (*5*). Clementine UV/VIS multispectral (415, 750, 900, 950, and 1000 nm) data with a spatial resolution of 118 m per pixel were used to compute TiO_2 and FeO contents, applying the algorithm in (*74*). Kaguya MI data with the same bands but higher spatial resolution (20 m per pixel) were used to assess the Al_2O_3, CaO, FeO, MgO, and TiO_2 contents (Fig. 6, C and D) and Mg# based on (*32*). Th abundances were based on Lunar Prospector GRS data, with a spatial resolution of 0.5° per pixel (*75*). The mineralogy (HCP, LCP, OLV, and PLG) was also obtained from the Kaguya MI data, using a lookup table technique for spectral unmixing (*30*, *31*). On the basis of the obtained mineralogy, PLG-LCP-HCP and PLG-PYX-OLV ternary diagrams were used to determine their lithologies (Fig. 6, A and B).

Impact mixing modeling

On the basis of the key source crater composition, primary ejecta thickness, and their formation ages, impact mixing models were applied to predict the composition and mineralogy of CE-6 soils (Fig. 6, A to D) and the age of impact materials (Fig. 5, A to C). The regolith gardening model in (*76*) was used to evaluate the mixing process. The regolith overturn depth at 99% probability is $\Lambda = 3.45 \times 10^{-5}\, t^{0.47}$ (at least one overturn, Λ is the reworking depth in meters, t is reworking time in years), which means the top ~95 cm of CE-6 regolith was mixed. For the young and old estimation models, the total ejecta thickness is ~93 and ~82 cm, respectively. Therefore, we could regard all ejecta as mixed and predicted the TiO_2 (2.4/2.6 wt %), FeO (13.5/14.0 wt %), Al_2O_3 (17.9/18.0 wt %), CaO (12.4/12.5 wt %), MgO (9.1/9.0 wt %), Th (2.0/2.0 ppm) contents, and Mg# (57.3/56.1) of CE-6 soils by a weighted-by-volume mixing model (Fig. 6, C and D), in addition to PLG (47.5/47.1 vol %), LCP (24.8/24.0 vol %), HCP (20.2/21.0 vol %), and OLV (7.5/7.9 vol %) abundances (Fig. 6, A and B). The values before and after "/" represent values obtained using the age of young and old estimation models (see above). All these elemental and mineralogical contents were close to the sample results (Fig. 6, A to D). This mixing model also constrained local mare (54.0/61.3 vol %), distant mare (0.2/0.3 vol %), and nonmare material (45.7%/38.4 vol %) abundances at the CE-6 site. The age distribution of ejecta was established similarly. With age and thickness of ejecta estimated above, we constructed the impact history of key impact events (>2 vol % local mare materials or >1 mm nonmare materials) (Fig. 5, A to C), in comparison with CE-5 impact material analyses both using impacting models (*17*) and laboratorial isotopic dating of the returned samples (Fig. 5D) (*65*), showing a high level of agreement (table S5).

CE-6 lunar samples

A total of 1000 mg of CE-6 sample CE6C0500 (YJFM002) from CNSA was used to determine the composition and mineral contents of the CE-6 site. These samples were collected by a robotic arm at the

Downloaded from https://www.science.org on November 18, 2026

surface (Fig. 2C), from a depth of ≤3 cm. Drilling samples were not used because of the difficulty in making comparisons with remote sensing datasets. Soil particles ≥50 μm were picked from the bulk soil, mounted in epoxy (CE-6 Clast Mount 1–9), and then polished and carbon-coated for petrological analyses. To better represent the bulk composition, six soil epoxy mounts (CE-6 Soil Mount 1–6) were made following the same procedure.

After that, the TIMA (TIMA3 X GMH) was used to automatically determine the mineralogy of each mount. This approach has the advantage of investigating a huge number of particles simultaneously. The TIMA system comprises a TESCAN MIRA3 Schottky field-emission scanning electron microscope and four high-flux energy-dispersive x-ray spectroscopy (EDS) detectors. The high-resolution mapping x-ray scanning acquisition mode was used, with x-ray counts set to 20,000, pixel spacing of backscattered electron (BSE) set to 1 μm, and dot spacing of EDS set to 3 μm. The measurements were conducted in a high-vacuum environment, with an acceleration voltage of 25 kV, a beam current of 9 nA, and a working distance of 15 mm. The beam and BSE signals were calibrated by a built-in platinum Faraday cup, and EDS signals by an Mn standard. TIMA software 2.11.0 was used to match the measured BSE and EDS data with existing databases (*77*) to obtain mineral phases (figs. S6 and S7), abundances, and compositions (table S7). In total, 1092 large clasts ≥50 μm and 2,935,175 soil particles ≥1 μm were analyzed. PYXs were classified into HCP and LCP because pigeonite and orthopyroxene are indistinguishable in spectroscopy. A total of 40,908 PYXs and 16,150 PLGs (major oxides = 98 to 102 wt %) were used to analyze their Mg# and An# after calibrated by EPMA data (Fig. 6, E and F). The major element compositions of each mount (table S7) were computed on the basis of the modal abundance of constituent minerals and their compositions. More details about the TIMA configuration and data processing can be found in (*37*, *77*).

CE-4 VNIS and CE-6 LMS

CE-4 and CE-6 both carried visible and infrared spectrometers. The VNIS (0.45 to 2.4 μm) is onboard Yutu-2 rover of CE-4, installed at a height of 0.695 m (Fig. 2A). It consists of a VIS/NIR channel [450 to 950 nm, 2.4 to 6.5 nm, signal-to-noise ratio (SNR) ≥33 dB], and a short-wave infrared spectrometer (SWIR) (900 to 2400 nm, spectral resolution = 3.6 to 9.6 nm, SNR ≥31 dB) (*35*). In detection mode, it collects VIS/NIR images [field of view (FOV) = 8.5° × 8.5°] and spectral information in the SWIR channel (Ø3.58°). For typical observations (fig. S10), the red circle represents the FOV of SWIR, centered at (98, 127.5) of the VIS/NIR image (*35*). The LMS (0.48 to 3.2 μm) was onboard the CE-6 lander (Fig. 2C), whose detection capability covered the sampling area (Fig. 2, D and E). It was installed at ~1.4 m above the surface, with an FOV of 4.17 × 4.17°. LMS has four channels: VIS (480 to 950 nm), NIR (900 to 1450 nm), SWIR (1400 to 2300 nm), and mid-wave infrared (MWIR) (2200 to 3200 nm) (*36*). The VIS/NIR and SWIR/MWIR channels have SNR >30 dB and >70 dB, respectively (*36*). In full-view multispectral mode, LMS acquired spectral images at 485, 560, 640, 750, 850, and 900 nm (Fig. 2E). In all-band hyperspectral mode, LMS obtained VIS images and three infrared-channel spectra of the entire FOV (fig. S11).

In this study, level 2B data from CE-4 VNIS and CE-6 LMS were used after dark current, flat-field, temperature, radiometric, and geometric corrections (*35*, *36*). The irradiance spectra were converted to reflectance divided by the solar irradiance. The obtained spectra were normalized to the NIR channel. In total, 36 CE-4 VNIS (table S9 and fig. S10) were used. Thirty spectra were obtained from soil targets (red dots, Fig. 2B) and six (CE4-D0015, CE4-D0107, CE4-0150, CE4-D0168, CE4-D0177, and CE4-D0239) were obtained from rock targets (yellow dots, Fig. 2B). VNIS data after 05 April 2022 were not used because of hardware aging of Yutu-2. For CE-6 LMS, 180 measurements were made by the full-view multispectral mode before sampling and mosaicked (Fig. 2, D and E). Fourteen spectra were collected by the all-band hyperspectral mode (table S10 and fig. S11). CE6-D0003 and CE6-D0017/CE6-D0022 were obtained from the sampling area before and after sampling operations (fig. S11). CE6-D0017/CE6-D0022 were not used because of large shadows. CE6-D0014, CE6-D0019, CE6-D0020, and CE6-D0023 investigated the same area.

Chandrayaan-1 M^3

M^3 is a push-broom imaging spectrometer (0.43 to 3.0 μm) onboard Chandrayaan-1. M^3 had two measurement modes, i.e., target mode and global mode. Because of various observing conditions, M^3 data were subdivided into five optical periods, each with relatively uniform thermal and observing conditions. Among all optical periods, OP2C1 and OP2C2 have the broadest coverage of SPA. Thus, OP2C1 and OP2C2 Global Mode reflectance data (spatial resolution of 140 × 280 m per pixel, spectral resolution of 20 nm) were used, which underwent radiometric, geometrical, thermal, photometrical, and ground truth calibrations (*78*).

OP2C1 and OP2C2 data were mosaicked to obtain the spectral features of the SPA basin (Figs. 1C; 3, A to C; and 8, A and B; and fig. S13, E to H). In addition, individual spectra were extracted from fresh small craters on Apollo western peak ring and SPACA central peaks (Bhabha, Stoney, Finsen, and White craters; Bose crater was not included because of lacking M^3 coverage) (fig. S12) to obtain their absorption features, PYX compositions, and Mg# (see below). Small fresh craters excavated subsurface immature materials that could mitigate space weathering effects. The spectra of mare basalts in the Von Kármán crater and Southern Apollo basin were also extracted from small fresh craters surrounding the landing sites (fig. S12) to compare with in situ data. The extracted mare spectra better represent pristine basalts (*7*, *8*) instead of the mixed soil signal of the landing site. All M^3 spectrum extraction points are shown in fig. S12 and listed in table S11. They were analyzed using the approach described below.

Hyperspectral analyses

CE-4 VNIS, CE-6 LMS, and Chandrayaan-1 M^3 hyperspectral data were processed using the approach in (*37*). All spectra were smoothed by the Savitzky-Golay filter, and the continuum was removed by the convex-hull method. BC1 and BC2 centers were calculated by finding the local minima between 800 to 1200 nm and 1700 to 2,500 nm in the continuum-removed spectra. The band centers of typical lunar minerals (Mg-OPX, Fe-OPX, low-Ca CPX, high-Ca CPX, and Wo50-PYX) (*38*) were computed using the same method for comparison (Fig. 7, A to C). BC2 is sensitive to Mg#. Mg^{2+} tends to occupy the PYX M1 octahedral site, which shifts BC1 (<950 nm) and BC2 (<2000 nm) to shorter wavelengths, in contrast to Ca^{2+} and Fe^{2+}, which shift to longer wavelengths (>2000 nm). One-dimensional KDE density analysis of BC2 was conducted on the spectra of Von Kármán mare basalt, Apollo southern mare basalt, Finsen central peak, Chaffee S, as well as CE-4 VNIS (soil and rock)

Downloaded from https://www.science.org on November 18, 2026

and CE-6 LMS (soil) data, to compare their absorption peaks and evaluate the degree of mixing between both landing sites (Fig. 7, A and B).

The PYX compositions (Wo and Fs) (table S11) were evaluated on the basis of the computed BC1 and BC2 of the extracted spectra using the method in (*40*)

$$Wo = \begin{cases} 347.9 * BC1 - 313.6 \ (Fs < 10) \\ 456.2 * BC1 - 416.9 \ (10 \le Fs < 25) \\ 418.9 * BC1 - 380.9 \ (25 \le Fs \le 50) \end{cases}$$

$$F_s = \begin{cases} 268.2 * BC2 - 483.7 \ (Wo < 11) \\ 57.5 * BC2 - 72.7 \ (11 \le Wo < 30) \\ -12.9 * BC2 + 45.9 \ (30 \le Wo \le 45) \\ -118.0 * BC2 + 278.5 \ (Wo > 45) \end{cases}$$

A lookup table technique was used to constrain the major mineral abundances (HCP, LCP, OLV, and PLG) and Mg#. It is based on a synthesized spectral library calculated by the Hapke model. We followed the same procedure as in (*79*), considering Mg# of the modeled spectra. Spectra were fitted over the wavelength range of 600 to 1400 nm, which best matches the in situ hyperspectral data (*80*). According to sensitivity tests, this approach has an accuracy of <3 and <6 vol % for mafic minerals and PLG, respectively, and <10 for Mg#. More details about the spectral unmixing can be found in text S3. Six representative examples are shown in fig. S14. Last, the obtained Mg# and PYX Wo, Fs values were plotted with PYX compositions from Mg-suite, Apollo mission impactites, and CE-6 noritic clasts to better understand their origin (Fig. 7, D to F, and fig. S8).

Supplementary Materials

The PDF file includes:

Supplementary Text S1 to S4
Figs. S1 to S16
Legends for tables S1 to S11
References

Other Supplementary Material for this manuscript includes the following:

Tables S1 to S11

REFERENCES

1. G. A. Neumann, M. T. Zuber, M. A. Wieczorek, J. W. Head, D. M. H. Baker, S. C. Solomon, D. E. Smith, F. G. Lemoine, E. Mazarico, T. J. Sabaka, S. J. Goossens, H. J. Melosh, R. J. Phillips, S. W. Asmar, A. S. Konopliv, J. G. Williams, M. M. Sori, J. M. Soderblom, K. Miljković, J. C. Andrews-Hanna, F. Nimmo, W. S. Kiefer, Lunar impact basins revealed by gravity recovery and interior laboratory measurements. *Sci. Adv.* **1**, e1500852 (2015).
2. Y. Wang, B. Wu, H. Xue, X. Li, J. Ma, An improved global catalog of lunar impact craters (≥1 km) with 3D morphometric information and updates on global crater analysis. *J. Geophys. Res. Planets* **126**, e2020JE006728 (2021).
3. N. Zhang, M. Ding, M.-H. Zhu, H. Li, H. Li, Z. Yue, Lunar compositional asymmetry explained by mantle overturn following the South Pole–Aitken impact. *Nat. Geosci.* **15**, 37–41 (2022).
4. R. I. Citron, D. E. Smith, S. T. Stewart, L. L. Hood, M. T. Zuber, The South Pole-Aitken basin: Constraints on impact excavation, melt, and ejecta. *Geophys. Res. Lett.* **51**, e2024GL110034 (2024).
5. D. P. Moriarty, C. M. Pieters, The character of South Pole-Aitken basin: Patterns of surface and subsurface composition. *J. Geophys. Res. Planets* **123**, 729–747 (2018).
6. B. Jolliff, N. Petro, D. Moriarty, R. Watkins, J. Head III, R. Potter, Sample return from the Moon's South Pole-Aitken basin. *Bull. Am. Astron. Soc.* **53**, 290 (2021).
7. J. Huang, Z. Xiao, J. Flahaut, M. Martinot, J. Head, X. Xiao, M. Xie, L. Xiao, Geological characteristics of Von Kármán crater, northwestern South Pole-Aitken basin: Chang'E-4 landing site region. *J. Geophys. Res. Planets* **123**, 1684–1700 (2018).
8. Y. Qian, J. Head, J. Michalski, X. Wang, C. H. van der Bogert, H. Hiesinger, L. Sun, W. Yang, L. Xiao, X. Li, G. Zhao, Long-lasting farside volcanism in the Apollo basin: Chang'e-6 landing site. *Earth Planet. Sci. Lett.* **637**, 118737 (2024).
9. Q. Zhou, W. Yang, Z. Chu, H. Zhu, S. Yang, X. Zeng, D.-S. Xue, L.-H. Jia, G. Zhang, H. Zhang, Y. Lin, H. Zhang, H.-C. Tian, P. Peng, D.-P. Zhang, L. Gu, C. Li, F.-Y. Wu, Ultra-depleted mantle source of basalts from the South Pole–Aitken basin. *Nature* **643**, 371–375 (2025).
10. Z. Cui, Q. Yang, Y.-Q. Zhang, C. Wang, H. Xian, Z. Chen, Z. Xiao, Y. Qian, J. W. Head, C. R. Neal, L. Xiao, F. Luo, J. Chen, P. He, Y. Cao, Q. Zhou, F. Huang, L. Chen, B. Wei, J. Wang, Y.-N. Yang, S. Li, Y. Yang, X. Lin, J. Zhu, L. Zhang, Y.-G. Xu, A sample of the Moon's far side retrieved by Chang'e-6 contains 2.83-billion-year-old basalt. *Science* **386**, 1395–1399 (2024).
11. Q. W. L. Zhang, M.-H. Yang, Q.-L. Li, Y. Liu, Z.-Y. Yue, Q. Zhou, L.-Y. Chen, H.-X. Ma, S.-H. Yang, X. Tang, G.-L. Zhang, X. Ren, X.-H. Li, Lunar farside volcanism 2.8 billion years ago from Chang'e-6 basalts. *Nature* **643**, 356–360 (2025).
12. D. M. Hurwitz, D. A. Kring, Differentiation of the South Pole–Aitken basin impact melt sheet: Implications for lunar exploration. *J. Geophys. Res. Planets* **119**, 1110–1133 (2014).
13. V. L. Sharpton, Outcrops on lunar crater rims: Implications for rim construction mechanisms, ejecta volumes and excavation depths. *J. Geophys. Res. Planets* **119**, 154–168 (2014).
14. R. J. Pike, Ejecta from large craters on the Moon: Comments on the geometric model of McGetchin et al. *Earth Planet. Sci. Lett.* **23**, 265–271 (1974).
15. N. E. Petro, C. M. Pieters, Surviving the heavy bombardment: Ancient material at the surface of South Pole-Aitken Basin. *J. Geophys. Res. Planets* **109**, E06004 (2004).
16. Y. Lu, Y. Wu, G. G. Michael, J. Ma, W. Cai, N. Qin, Chronological sequence of Chang'E-4 landing zone within Von Kármán crater. *Icarus* **354**, 114086 (2021).
17. Y. Qian, L. Xiao, J. W. Head, C. Wöhler, R. Bugiolacchi, T. Wilhelm, S. Althoff, B. Ye, Q. He, Y. Yuan, S. Zhao, Copernican-aged (<200 Ma) impact Ejecta at the Chang'e-5 landing site: Statistical evidence from crater morphology, morphometry, and degradation models. *Geophys. Res. Lett.* **48**, e2021GL095341 (2021).
18. S. Yamamoto, R. Nakamura, T. Matsunaga, Y. Ogawa, Y. Ishihara, T. Morota, N. Hirata, M. Ohtake, T. Hiroi, Y. Yokota, J. Haruyama, Massive layer of pure anorthosite on the Moon. *Geophys. Res. Lett.* **39**, L13201 (2012).
19. C. Orgel, G. Michael, C. I. Fassett, C. H. van der Bogert, C. Riedel, T. Kneissl, H. Hiesinger, Ancient bombardment of the inner Solar System: Reinvestigation of the "fingerprints" of different impactor populations on the lunar surface. *J. Geophys. Res. Planets* **123**, 748–762 (2018).
20. H. Hiesinger, C. H. van der Bogert, J. H. Pasckert, N. Schmedemann, M. S. Robinson, B. Jolliff, N. Petro, New crater size-frequency distribution measurements of the South Pole-Aitken basin (Lunar and Planetary Institute, Houston, 2012); https://lpi.usra.edu/meetings/lpsc2012/pdf/2863.pdf, Abstract #2863.
21. A. A. Nemchin, T. Long, B. L. Jolliff, Y. Wan, J. F. Snape, R. Zeigler, M. L. Grange, D. Liu, M. J. Whitehouse, N. E. Timms, F. Jourdan, Ages of lunar impact breccias: Limits for timing of the Imbrium impact. *Geochemistry* **81**, 125683 (2021).
22. Z. Yue, M. Yang, M. Jia, G. Michael, K. Di, S. Gou, J. Liu, Refined model age for Orientale basin derived from zonal crater dating of its ejecta. *Icarus* **346**, 113804 (2020).
23. K. H. Joy, N. Wang, J. F. Snape, A. Goodwin, J. F. Pernet-Fisher, M. J. Whitehouse, Y. Liu, Y. T. Lin, J. R. Darling, P. Tar, R. Tartèse, Evidence of a 4.33 billion year age for the Moon's South Pole–Aitken basin. *Nat. Astron.* **9**, 55–65 (2025).
24. M. Barboni, D. Szymanowski, B. Schoene, N. Dauphas, Z. J. Zhang, X. Chen, K. D. McKeegan, High-precision U-Pb zircon dating identifies a major magmatic event on the Moon at 4.338 Ga. *Sci. Adv.* **10**, eadn9871 (2025).
25. I. Garrick-Bethell, K. Miljković, H. Hiesinger, C. H. van der Bogert, M. Laneuville, D. L. Shuster, D. G. Korycansky, Troctolite 76535: A sample of the Moon's South Pole-Aitken basin? *Icarus* **338**, 113430 (2020).
26. D. E. Wilhelms, J. F. McCauley, N. J. Trask, The geologic history of the Moon (1987); https://doi.org/10.3133/pp1348.
27. C. Li, H. Hu, M.-F. Yang, J. Liu, Q. Zhou, X. Ren, B. Liu, D. Liu, X. Zeng, W. Zuo, G. Zhang, H. Zhang, S. Yang, Q. Wang, X. Deng, X. Gao, Y. Su, W. Wen, Z. Ouyang, Nature of the lunar far-side samples returned by the Chang'E-6 mission. *Natl. Sci. Rev.* **11**, nwae328 (2024).
28. H. Cao, J. Chen, X. Lu, J. Kong, L. Qiao, C. Yin, C. Liu, H. Qu, X. Fu, Y. Xin, Z. Ling, Impact-induced mixing generated the stratified soils of the Lunar South Pole Aitken basin. *Commun. Earth Environ.* **6**, 522 (2025).
29. Z. Wang, Y. Li, J. Li, K. Zong, Z. She, Q. He, J. Zhao, W. Zhang, J. Zheng, F. Pan, T. Luo, K. Crnobrnja, X. Chen, L. Xiao, Z. Hu, X. Wu, Y. Liu, F. Moynier, Chemical compositions of Chang'e-6 lunar soil and substantial addition of noritic crust ejecta from Apollo basin. *Geology* **53**, 557–561 (2025).

Downloaded from https://www.science.org on November 18, 2026

30. M. Lemelin, P. G. Lucey, K. Miljković, L. R. Gaddis, T. Hare, M. Ohtake, The compositions of the lunar crust and upper mantle: Spectral analysis of the inner rings of lunar impact basins. *Planet. Space Sci.* **165**, 230–243 (2019).
31. M. Lemelin, P. G. Lucey, A. Camon, Compositional maps of the lunar polar regions derived from the Kaguya spectral profiler and the lunar orbiter laser altimeter data. *Planet. Sci. J.* **3**, 63 (2022).
32. L. Zhang, X. Zhang, M. Yang, X. Xiao, D. Qiu, J. Yan, L. Xiao, J. Huang, New maps of major oxides and Mg # of the lunar surface from additional geochemical data of Chang'E-5 samples and KAGUYA multiband imager data. *Icarus* **397**, 115505 (2023).
33. C. K. Shearer, S. M. Elardo, N. E. Petro, L. E. Borg, F. M. McCubbin, Origin of the lunar highlands Mg-suite: An integrated petrology, geochemistry, chronology, and remote sensing perspective. *Am. Mineral.* **100**, 294–325 (2015).
34. B. Su, Y. Chen, Z. Wang, D. Zhang, H. Chen, S. Gou, Z. Yue, Y. Liu, J. Yuan, G. Tang, S. Guo, Q. Li, Y.-T. Lin, X.-H. Li, F.-Y. Wu, South Pole–Aitken massive impact 4.25 billion years ago revealed by Chang'e-6 samples. *Natl. Sci. Rev.* **12**, nwaf103 (2025).
35. R. Xu, H. Lin, M. Wang, B. Liu, W. Yan, C. Liu, G. Lv, L. Yuan, C. Li, R. Wang, D. Liu, Y. Yang, Z. Jiang, B. Yang, L. Wang, J. Xu, J. Li, Z. He, In-flight calibration of visible and near-infrared imaging spectrometer (VNIS) onboard Chang'E-4 unmanned lunar rover. *IEEE Trans. Geosci. Remote Sens.* **60**, 5542311 (2022).
36. R. Xu, C. Li, L. Yuan, G. Lv, S. Xu, F. Li, J. Jin, Z. Wang, W. Pan, R. Wang, M. Wang, J. Xie, J. Yang, J. Wang, Z. He, Lunar mineralogical spectrometer on Chang'E-5 mission. *Space Sci. Rev.* **218**, 41 (2022).
37. Y. Qian, Z. She, Q. He, L. Xiao, Z. Wang, J. W. Head, L. Sun, Y. Wang, B. Wu, X. Wu, B. Luo, K. Cao, Y. Li, M. Dong, W. Song, F. Pan, J. Michalski, B. Ye, J. Zhao, S. Zhao, J. Huang, J. Zhao, J. Wang, K. Zong, Z. Hu, Mineralogy and chronology of the young mare volcanism in the Procellarum-KREEP-Terrane. *Nat. Astron.* **7**, 287–297 (2023).
38. R. L. Klima, C. M. Pieters, M. D. Dyar, Spectroscopy of synthetic Mg-Fe pyroxenes I: Spin-allowed and spin-forbidden crystal field bands in the visible and near-infrared. *Meteorit. Planet. Sci.* **42**, 235–253 (2007).
39. M. J. Cintala, R. A. F. Grieve, Scaling impact melting and crater dimensions: Implications for the lunar cratering record. *Meteorit. Planet. Sci.* **33**, 889–912 (1998).
40. M. J. Gaffey, Mineralogy of asteroids. *AIP Conf. Proc.* **1386**, 129–169 (2011).
41. J. Gross, A. Hilton, T. C. Prissel, J. B. Setera, R. L. Korotev, A. Calzada-Diaz, Geochemistry and petrogenesis of Northwest Africa 10401: A new type of the Mg-suite rocks. *J. Geophys. Res. Planets* **125**, e2019JE006225 (2020).
42. Z. Wang, W. Tian, W.-R. Wang, T. C. Prissel, Y. Di, Y. Qian, P.-P. Liu, W. Fa, A. Su, Genesis and timing of KREEP-free lunar Mg-suite magmatism indicated by the first norite meteorite Arguin 002. *Commun. Earth Environ.* **6**, 170 (2025).
43. S. Yamamoto, H. Nagaoka, M. Ohtake, M. Kayama, Y. Karouji, Y. Ishihara, J. Haruyama, Lunar mantle composition based on spectral and geologic analysis of low-Ca pyroxene- and olivine-rich rocks exposed on the lunar surface. *J. Geophys. Res. Planets* **128**, e2023JE007817 (2023).
44. D. Guo, Y. Bao, X. Wu, S. Li, Y. Liu, Y. Yang, Y. Xu, F. Zhang, J. Liu, Y. Zou, Crystalline ferroan anorthosite identified in the lunar Apollo basin. *J. Geophys. Res. Planets* **130**, e2024JE008690 (2025).
45. M. A. Wieczorek, G. A. Neumann, F. Nimmo, W. S. Kiefer, G. J. Taylor, H. J. Melosh, R. J. Phillips, S. C. Solomon, J. C. Andrews-Hanna, S. W. Asmar, A. S. Konopliv, F. G. Lemoine, D. E. Smith, M. M. Watkins, J. G. Williams, M. T. Zuber, The crust of the Moon as seen by GRAIL. *Science* **339**, 671 (2013).
46. L. M. Jozwiak, J. W. Head, M. T. Zuber, D. E. Smith, G. A. Neumann, Lunar floor-fractured craters: Classification, distribution, origin and implications for magmatism and shallow crustal structure. *J. Geophys. Res. Planets* **117**, E11005 (2012).
47. Q. Deng, Z. Xiao, Y. Wu, P. Ma, W. Cao, Y. Wang, Y. Ma, F. Luo, F. Li, Magmatic dikes in the Chang'e-6 sampling area. *Earth Planet. Sci. Lett.* **660**, 119350 (2025).
48. R. W. K. Potter, J. W. Head, D. Guo, J. Liu, L. Xiao, The Apollo peak-ring impact basin: Insights into the structure and evolution of the South Pole–Aitken basin. *Icarus* **306**, 139–149 (2018).
49. J. Chen, L. Zhang, Z. Cui, Z. Chen, Z. Xiao, F. Luo, Y. Qian, Y.-Q. Zhang, C. Wang, J. Wang, Q. Yang, P. He, L. Chen, F. Huang, H. Xian, K. H. Joy, J. W. Head, C. R. Neal, Y.-G. Xu, KREEP-like lithologies in the South Pole–Aitken basin reworked by the Apollo basin impact at 4.16 Ga. *Nat. Astron.* **9**, 1638–1647 (2025).
50. T. Long, A. Nemchin, X. Che, S. Xie, Z. Li, C. Wang, C. Yang, D. Liu, Modification of crust and mantle in the South Pole Aitken region of the Moon. *Commun. Earth Environ.* **7**, 802 (2026).
51. J. Zheng, Q. He, Z. Wang, J. Huang, J. F. Pernet-Fisher, Y. Li, X. Chen, K. Zong, I. Baziotis, L. Xiao, Z. She, Petrogenesis of lunar farside highland lithologies: Implications for lunar crust formation. *Astrophys. J.* **992**, 83 (2025).
52. W. Du, J. Yang, The Moon's early magmatic activities: From the perspective of lunar alkali-suite and Mg-suite samples. *Space Sci. Technol.* **4**, 0118 (2024).
53. W.-F. Zhang, L. Zhang, M. Lin, F. Jourdan, J.-J. Wang, Y.-Q. Zhang, J.-Y. Chen, D.-W. Zheng, P.-L. He, F. Su, H.-Y. He, H.-N. Qiu, X.-J. Bai, X.-P. Xia, M. Xiao, Y.-D. Jiang, J.-J. Li, J. Zhang, L.-K. Yang, F.-F. Huang, B. Wei, J.-Z. Wang, Q. Zhou, Y.-H. Cao, Z.-X. Cui, Q. Yang, L.-L. Chen, Y.-G. Xu, The bombardment history on the lunar farside revealed by 40Ar/39Ar geochronology of Chang'e-6 impact melt rocks. *Sci. Adv.* **12**, eaee8718 (2026).
54. F. Nimmo, T. Kleine, A. Morbidelli, Tidally driven remelting around 4.35 billion years ago indicates the Moon is old. *Nature* **636**, 598–602 (2024).
55. B. L. Jolliff, J. J. Gillis, L. A. Haskin, R. L. Korotev, M. A. Wieczorek, Major lunar crustal terranes: Surface expressions and crust-mantle origins. *J. Geophys. Res. Planets* **105**, 4197–4216 (2000).
56. Z. Chen, L. Zhang, J. Chen, C. Wang, J. Wang, Z. Cui, Z. Zou, P. He, Y. Cao, Q. Zhou, L. Chen, Y.-Q. Zhang, Y.-G. Xu, Abundant non-mare components in the Chang'e-6 lunar regolith: Constraints from plagioclase fragments and impact glasses. *J. Geophys. Res. Planets* **130**, e2025JE008976 (2025).
57. B.-W. Wang, L.-Y. Chen, Q.-L. Li, J. W. Delano, J.-X. Sun, Y. Chen, H.-X. Ma, D. Zhang, S.-T. Wu, S. Gou, X.-H. Li, F.-Y. Wu, KREEP materials recorded in impact glasses of Chang'e-6 regolith returned from the South Pole-Aitken basin. *Fundam. Res.* **6**, 1650–1659 (2026).
58. S. Ji, C. Deliang, Z. Zhiwei, Z. Yingnan, Q. Liping, Petrographic study of lithic fragments in Chang'e-6 surface regolith. *Solid Earth Sci.* **10**, 100275 (2025).
59. T. C. Prissel, N. Zhang, C. R. M. Jackson, H. Li, Rapid transition from primary to secondary crust building on the Moon explained by mantle overturn. *Nat. Commun.* **14**, 5002 (2023).
60. M. A. Ivanov, H. Hiesinger, C. H. van der Bogert, C. Orgel, J. H. Pasckert, J. W. Head, Geologic history of the northern portion of the South Pole-Aitken basin on the Moon. *J. Geophys. Res. Planets* **123**, 2585–2612 (2018).
61. C. M. Fortezzo, P. D. Spudis, S. L. Harrel, Release of the digital unified global geologic map of the Moon at 1:5,000,000-scale, *51st Lunar and Planetary Science Conference* (2020) Abstract #2760.
62. C. Wang, Y. Qian, J. Wang, L. Liu, L. Zhang, Z. Chen, J. Chen, G. Zhu, X. Tu, Z. Cui, Q. Yang, Y.-Q. Zhang, P. He, Y. Cao, H. Xian, J. W. Head, Y.-G. Xu, The source and thermal driver of young (<3.0 Ga) lunar volcanism. *Sci. Adv.* **11**, eadv9085 (2025).
63. L. Xu, L. Qiao, M. Xie, Y. Wang, M.-H. Zhu, J. Yan, Local stratigraphy, and foreign ejecta materials at the Chang'e-6 landing site: Constraints on the provenance of samples returned from the Moon's farside. *Geophys. Res. Lett.* **51**, e2024GL111311 (2024).
64. M. Zhang, W. Fa, B. Jia, Provenance and evolution of lunar regolith at the Chang'e-6 sampling site. *Nat. Astron.* **9**, 813–823 (2025).
65. T. Long, Y. Qian, M. D. Norman, K. Miljkovic, C. Crow, J. W. Head, X. Che, R. Tartèse, N. Zellner, X. Yu, S. Xie, M. Whitehouse, K. H. Joy, C. R. Neal, J. F. Snape, G. Zhou, S. Liu, C. Yang, Z. Yang, C. Wang, L. Xiao, D. Liu, A. Nemchin, Constraining the formation and transport of lunar impact glasses using the ages and chemical compositions of Chang'e-5 glass beads. *Sci. Adv.* **8**, eabq2542 (2022).
66. T. Krüger, S. Hergarten, T. Kenkmann, Deriving morphometric parameters and the simple-to-complex transition diameter from a high-resolution, global database of fresh lunar impact craters (D ≥ ~ 3 km). *J. Geophys. Res. Planets* **123**, 2667–2690 (2018).
67. K. Terada, T. Morota, M. Kato, Asteroid shower on the Earth-Moon system immediately before the Cryogenian period revealed by KAGUYA. *Nat. Commun.* **11**, 3453 (2020).
68. M. R. Kirchoff, S. Marchi, W. F. Bottke, C. R. Chapman, B. Enke, Suggestion that recent (≤ 3 Ga) flux of kilometer and larger impactors in the Earth-Moon system has not been constant. *Icarus* **355**, 114110 (2021).
69. G. Neukum, B. A. Ivanov, W. K. Hartmann, Cratering records in the inner Solar System in relation to the lunar reference system, in *Chronology and Evolution of Mars*, R. Kallenbach, J. Geiss, W. K. Hartmann, Eds. (Springer, 2001), pp. 55–86.
70. Z. Yue, K. Di, W. Wan, Z. Liu, S. Gou, B. Liu, M. Peng, Y. Wang, M. Jia, J. Liu, Z. Ouyang, Updated lunar cratering chronology model with the radiometric age of Chang'e-5 samples. *Nat. Astron.* **6**, 541–545 (2022).
71. M. Xie, M.-H. Zhu, Z. Xiao, Y. Wu, A. Xu, Effect of topography degradation on crater size-frequency distributions: Implications for populations of small craters and age dating. *Geophys. Res. Lett.* **44**, 10171–10179 (2017).
72. C. I. Fassett, B. J. Thomson, Crater degradation on the lunar maria: Topographic diffusion and the rate of erosion on the Moon. *J. Geophys. Res. Planets* **119**, 2255–2271 (2014).
73. A. T. Basilevsky, On the evolution rate of small lunar craters, in *7th Lunar Science Conference* (Pergamon Press, 1976), pp. 1005–1020.
74. P. G. Lucey, D. T. Blewett, B. L. Jolliff, Lunar iron and titanium abundance algorithms based on final processing of Clementine ultraviolet-visible images. *J. Geophys. Res. Planets* **105**, 20297–20305 (2000).
75. T. H. Prettyman, J. J. Hagerty, R. C. Elphic, W. C. Feldman, D. J. Lawrence, G. W. McKinney, D. T. Vaniman, Elemental composition of the lunar surface: Analysis of gamma ray spectroscopy data from Lunar Prospector. *J. Geophys. Res. Planets* **111**, E12007 (2006).
76. E. S. Costello, R. R. Ghent, M. Hirabayashi, P. G. Lucey, Impact gardening as a constraint on the age, source, and evolution of ice on Mercury and the Moon. *J. Geophys. Res. Planets* **125**, e2019JE006172 (2020).
77. S. Xue, W. Song, Z. Guo, Y. Qian, K. Huang, C. Zhang, Q. Liu, X. Wang, L. Qiao, Q. Chen, D. Zhang, L. Chen, H. Yuan, G. Zhao, Mineralogy and provenance of the Chang'e-6 shoveled lunar samples. *Lithos* **516-517**, 108265 (2025).

Downloaded from https://www.science.org on November 18, 2026

78. R. O. Green, C. Pieters, P. Mouroulis, M. Eastwood, J. Boardman, T. Glavich, P. Isaacson, M. Annadurai, S. Besse, D. Barr, B. Buratti, D. Cate, A. Chatterjee, R. Clark, L. Cheek, J. Combe, D. Dhingra, V. Essandoh, S. Geier, J. N. Goswami, R. Green, V. Haemmerle, J. Head, L. Hovland, S. Hyman, R. Klima, T. Koch, G. Kramer, A. S. K. Kumar, K. Lee, S. Lundeen, E. Malaret, T. McCord, S. McLaughlin, J. Mustard, J. Nettles, N. Petro, K. Plourde, C. Racho, J. Rodriquez, C. Runyon, G. Sellar, C. Smith, H. Sobel, M. Staid, J. Sunshine, L. Taylor, K. Thaisen, S. Tompkins, H. Tseng, G. Vane, P. Varanasi, M. White, D. Wilson, The Moon Mineralogy Mapper (M3) imaging spectrometer for lunar science: Instrument description, calibration, on-orbit measurements, science data calibration and on-orbit validation. *J. Geophys. Res. Planets* **116**, 2011JE003797 (2011).
79. L. Sun, P. G. Lucey, Unmixing mineral abundance and Mg# with radiative transfer theory: Modeling and applications. *J. Geophys. Res. Planets* **126**, e2020JE006691 (2021).
80. H. Zhang, Y. Yang, Y. Yuan, W. Jin, P. G. Lucey, M.-H. Zhu, V. G. Kaydash, Y. G. Shkuratov, K. Di, W. Wan, B. Xu, L. Xiao, Z. Wang, B. Xue, In situ optical measurements of Chang'E-3 landing site in Mare Imbrium: 1. Mineral abundances inferred from spectral reflectance. *Geophys. Res. Lett.* **42**, 6945–6950 (2015).
81. W. Yan, X. Zeng, X. Ren, W. Chen, X. Gao, W. Zuo, B. Liu, Z. Zhang, Q. Fu, J. Liu, C. Li, Geological characteristics of Chang'E-6 landing area in micro-scale unveiled by new observation data. *Nat. Commun.* **16**, 4219 (2025).
82. D. Stöffler, G. Ryder, Stratigraphy and isotope ages of lunar geologic units: Chronological standard for the inner Solar System, in *Chronology and Evolution of Mars*, R. Kallenbach, J. Geiss, W. K. Hartmann, Eds. (Springer, 2001), pp. 9–54.
83. B. Hapke, *Theory of Reflectance and Emittance Spectroscopy* (Cambridge Univ. Press, ed. 2, 2012).
84. B. Hapke, Bidirectional reflectance spectroscopy: 4. The extinction coefficient and the opposition effect. *Icarus* **67**, 264–280 (1986).
85. J. F. Mustard, C. M. Pieters, Photometric phase functions of common geologic minerals and applications to quantitative analysis of mineral mixture reflectance spectra. *J. Geophys. Res. Solid Earth* **94**, 13619–13634 (1989).
86. M. Lemelin, P. G. Lucey, E. Song, G. J. Taylor, Lunar central peak mineralogy and iron content using the Kaguya Multiband Imager: Reassessment of the compositional structure of the lunar crust. *J. Geophys. Res. Planets* **120**, 869–887 (2015).
87. Y. Qian, J. Head, J. Michalski, S. Gong, W. Yang, Z. Wang, L. Xiao, X. Li, G. Zhao, Extensive intrusive magmatism in the lunar farside Apollo and South Pole–Aitken basins, Chang'e-6 landing site. *Astrophys. J. Lett.* **971**, L39 (2024).
88. D. Trang, J. J. Gillis-Davis, B. R. Hawke, The origin of lunar concentric craters. *Icarus* **278**, 62–78 (2016).
89. H. Frey, Previously unknown large impact basins on the Moon: Implications for lunar stratigraphy, in *Recent Advances and Current Research Issues in Lunar Stratigraphy*, W. A. Ambrose, D. A. Williams, Eds. (Geological Society of America, 2011), Special Paper 477; https://doi.org/10.1130/2011.2477(02).
90. X. Che, T. Long, A. Nemchin, S. Xie, L. Qiao, Z. Li, Y. Ban, R. Fan, C. Yang, D. Liu, Isotopic and compositional constraints on the source of basalt collected from the lunar farside. *Science* **387**, 1306–1310 (2025).
91. S. He, Y. Li, X. Zhu, J. Chen, Z. Li, T. Li, J. Zhong, J. Tan, Q. He, Z. Fu, Y. Zheng, J. Xing, Z. Shi, A relatively cool lunar farside mantle inferred from Chang'e-6 basalts and remote sensing. *Nat. Geosci.* **18**, 1103–1108 (2025).
92. D. Shen, S. Li, S. Li, Y. Xu, Y. Li, M. Li, D. Wang, R. Pang, Y. Zhang, Z. Han, Petrogenesis of Chang'E-6 basalts and implication for multi-episode volcanism in the lunar farside basin. *Earth Planet. Sci. Lett.* **659**, 119335 (2025).
93. C. Yin, J. Chen, X. Fu, H. Cao, X. Lu, Y. Liu, J. Li, S. Chi, X. Zeng, Z. Ling, Petrogenesis of Chang'e-6 basalts and implication for the young volcanism on the lunar farside. *Astrophys. J. Lett.* **981**, L2 (2025).
94. H. Zhang, W. Yang, D. Zhang, J. Hao, X. Liu, H. Zhu, R. N. Mitchell, L. Jia, Y. Fan, S. Wu, L. Gu, X. Tang, H.-C. Tian, J. Pei, Y. Lin, X.-H. Li, F.-Y. Wu, A more reduced mantle beneath the lunar South Pole–Aitken basin. *Nat. Commun.* **16**, 6985 (2025).

Acknowledgments: We thank the China National Space Administration (CNSA) for providing the Chang'e-6 samples and the Chang'e-4 and Chang'e-6 scientific data. We also thank the Ground Research and Application System (GRAS) for the support in analyzing the Chang'e-4 and Chang'e-6 scientific data. **Funding:** This research was funded by the HK RGC General Research Fund 17300526 (Y.Q. and M.T.), 17307025 (Y.Q. and M.T.), 17306623 (Y.Q. and J.L.), 17306324 (W.R.L.), and the Co-funding Mechanism on Joint Laboratories with the Chinese Academy of Sciences JLFS/P-702/24 (Y.Q., M.T., L.Z., J.C., W.Z., X.W., W.R.L., J.L., Y.G.X., and G.Z.). H.H. and C.H.v.d.B. were funded by the German Aerospace Agency (DLR) grant 50OW2402. **Author contributions:** Y.Q., Z.G., W.R.L., and G.Z. applied CE-6 samples from CNSA. Y.Q., W.S., Z.G., X.W., and W.R.L. conducted CE-6 sample experiments. Y.Q., J.H., M.T., H.H., C.v.d.B., L.S., and J.L. conducted remote sensing and in situ data analyses. Y.Q., J.H., H.H., C.vd.B., L.Z., J.C., W.Z., Z.L., N.D., and Y.G.X. conducted magmatic and impact history analyses. All authors wrote the manuscript. **Competing interests:** The authors declare that they have no competing interests. **Data, code, and materials availability:** Chang'e-4 and Chang'e-6 in situ data and Chang'e-2 orbital data are available through the China's Lunar and Planetary Data Release System (https://moon.bao.ac.cn). Chang'e-4 VNIS and Chang'e-6 LMS data are also available in tables S9 and S10. Chang'e-6 lunar sample (CE6C0500YJFM002) was applied from CNSA, according to the Notice of CNSA on the Distribution of Procedures for Requesting Lunar Samples. LROC Wide-Angle Camera, Narrow-Angle Camera, Lunar Prospector thorium abundance data, and Chandrayaan-1 Moon Mineralogy Mapper data are from NASA's Planetary Data System Geoscience Node (https://pds-geosciences.wustl.edu). The M^3 IDs used are listed in table S11. The LROC LOLA DEM and Clementine UVVIS FeO, TiO_2 data are available from the USGS's Astropedia (https://astrogeology.usgs.gov/search). The Kaguya Multiband Imager elemental abundance data are available through Zenodo (https://doi.org/10.5281/zenodo.7263319, https://doi.org/10.5281/zenodo.7263325, https://doi.org/10.5281/zenodo.7263426, https://doi.org/10.5281/zenodo.7263593, https://doi.org/10.5281/zenodo.7264329, https://doi.org/10.5281/zenodo.7264373). The Kaguya TC Morning and Ortho Map data are available through PDAP Kaguya Data Archive (https://legacy.darts.isas.jaxa.jp/app/pdap/selene/). The Kaguya Multiband Imager mineralogical abundance data are available through USGS's Astropedia (https://astrogeology.usgs.gov/search), as well as Zenodo (https://doi.org/10.5281/zenodo.7108163). The GRAIL crustal thickness is available through Zenodo (https://zenodo.org/records/997347). Craterstats2 is available through reie Universität Berlin (https://geo.fu-berlin.de/en/geol/fachrichtungen/planet/software/_content/software/craterstats.html). Figures were produced by ArcGIS, QGIS, Adobe Illustrator, or Python Matplotlib (https://matplotlib.org), or Plotly (https://plotly.com/python/). This study did not generate new materials.

Submitted 12 April 2026
Accepted 19 October 2026
Published 18 November 2026
10.1126/sciadv.aeh9798

Downloaded from https://www.science.org on November 18, 2026

ScienceAdvances

Postimpact evolution of the South Pole–Aitken basin revealed by Chang'e-4 and Chang'e-6

Yuqi Qian, Wenlei Song, James Head, Mingyu Tian, Zhuang Guo, Harald Hiesinger, Carolyn H. van der Bogert, Le Zhang, Jingyou Chen, Wanfeng Zhang, Ziqing Li, Lingzhi Sun, Xiangsong Wang, Wei-Ran Li, Jiacheng Liu, Nicolas Dauphas, Yi-Gang Xu, and Guochun Zhao

Sci. Adv. **12** (47), eaeh9798. DOI: 10.1126/sciadv.aeh9798

View the article online
https://www.science.org/doi/10.1126/sciadv.aeh9798
Permissions
https://www.science.org/help/reprints-and-permissions

Downloaded from https://www.science.org on November 18, 2026

Use of this article is subject to the Terms of service

Science Advances (ISSN 2375-2548) is published by the American Association for the Advancement of Science. 1200 New York Avenue NW, Washington, DC 20005. The title *Science Advances* is a registered trademark of AAAS.

Copyright © 2026 The Authors, some rights reserved; exclusive licensee American Association for the Advancement of Science. No claim to original U.S. Government Works. Distributed under a Creative Commons Attribution License 4.0 (CC BY).